Nonlinear flexural waves in fluid–filled elastic channels

N.P. Deacon[a,*], E.I. Părău[a], R. Purvis[a], R.J. Whittaker[a]

[a] *School of Mathematics, University of East Anglia, Norwich Research Park, Norwich NR4 7TJ, United Kingdom*

Abstract

Nonlinear waves on liquid sheets between thin infinite elastic plates are studied analytically and numerically. Linear and nonlinear models are used for the elastic plates coupled to the Euler equations for the fluid. One-dimensional time-dependent equations are derived based on a long-wavelength approximation. Inertia of the elastic plates is neglected, so linear perturbations are stable. Symmetric and mixed-mode travelling waves are found with the linear plate model and symmetric travelling waves are found for the nonlinear case. Numerical simulations are employed to study the evolution in time of initial disturbances and to compare the different models used. Nonlinear effects are found to decrease the travelling wave speed compared with linear models. At sufficiently large amplitude of initial disturbances, higher order temporal oscillations induced by nonlinearity can lead to thickness of the liquid sheet approaching zero.

Keywords: flexural waves, channel flow, nonlinear waves

1. Introduction

Interactions between fluids and elastic boundaries occur frequently in both natural and mechanical environments (Korobkin et al., 2011). Such problems are mathematically challenging, due the coupling between the moving fluid and the deformable boundary. In this paper we examine the flow of an inviscid fluid between two thin elastic plates. Examples of systems where similar types of waves arise include the pulmonary system (e.g. Grotberg, 1994; Walsh, 1995), in flat-plate-type fuel assemblies used in the cooling systems of nuclear reactors (e.g. Kim and Davis, 1995) and in energy-harvesting devices (see Tang (2007)).

The linear stability of similar fluid–elastic systems have been examined by many authors in the past. Walsh (1995) used shell theory to examine pipes with three different kinds of flow; internal, annular and planar. The internal flow was axisymmetric in a flexible pipe, the annular flow was axisymmetric, between a flexible inner shell and a rigid outer one, and the planar flow considered flow between a rigid plane and a flexible one. He found that, for inviscid flow, tubes where the displacements in both the axial and normal directions are considered together are unstable to long wave flutter, but stable if each are considered on their own. Nonlinear stability of fluid-loaded elastic plates was investigated by Peake (2001). De Langre and Ouvrard (1999) considered instabilities which arise in a flexural pipe, with a spring foundation and under tension, for the coupled mode.

De Langre (2002) expanded upon this work to allow both symmetric and antisymmetric perturbations, in a paper examining regions in which convective instabilities change to absolute instabilities and vice versa. More recently, the linear stability of a finite number of coupled parallel flexible plates in axial flow have been studied by Michelin and Llewellyn Smith (2009). Experiments on the flutter instability of assemblies of two or more parallel flexible cantilevered plates have been performed by Schouveiler and Eloy (2009). The coupled dynamics of two parallel cantilevered flexible plates of finite length in axial flow has been studied in Tang and Païdoussis (2009). Branches of nonlinear symmetric and antisymmetric travelling waves and

*Corresponding author. Tel.: +44 1603 456161
Email addresses: n.deacon@uea.ac.uk (N.P. Deacon), e.parau@uea.ac.uk (E.I. Părău), r.purvis@uea.ac.uk (R. Purvis)
URL: http://robert.mathmos.net/research/ (R.J. Whittaker)

other bifurcation branches for fluid sheets between thin elastic plates were also computed by Blyth et al. (2011).

In the absence of elastic walls, we recover the classical problem of plane liquid sheets. Squire (1953) studied the temporal instability of a plane liquid sheet moving through air. He showed that long waves were unstable, and the antisymmetric disturbances are less unstable than the symmetric ones. He also calculated the largest growing mode by considering the maximum value of the imaginary component of the frequency. The spatial instability equivalent was studied by Li (1993) for high flow velocities through a gaseous medium. He found the dispersion relation for antisymmetric and symmetric modes for different gas-to-liquid density ratios, and analysed growth rates of instabilities for different parameter values.

The linear stability analysis of thin planar liquid sheets was extended by Mehring and Sirignano (1999) by considering the fully nonlinear problem. They examined nonlinear symmetric and antisymmetric capillary waves by reducing the two-dimensional unsteady problem to a one-dimensional unsteady problem, assuming that the liquid sheet thickness is small compared with the wavelength of the disturbance. Numerical simulations were used to study the time evolution of the waves and differences were found compared with the linear case. Travelling waves were computed in the symmetric case. They also investigated the nonlinear deformation of semi-infinite sheets, forced periodically at one end.

In this paper we extend the Mehring and Sirignano (1999) method to study nonlinear symmetric and antisymmetric waves in fluid sheets between two infinite elastic walls. A system of one-dimensional unsteady equations is derived in three cases: a linear-flow–linear-plate model, a nonlinear-flow–linear-plate model and a nonlinear-flow–nonlinear-plate model. The plates are assumed inextensible and their inertia is neglected. In the third case the plates are modelled using the special Cosserat theory of hyperelastic shells, satisfying Khirchoff's hypothesis (see also Plotnikov and Toland (2011), Blyth et al. (2011)). Travelling waves are found in each case. The evolution in time of symmetric and antisymmetric waves is compared for different problems and the nonlinear effects are discussed.

In §2 we outline the problem and derive the governing equations before finding solutions to the linearised system in §3. Travelling waves are then sought numerically for the leading order curvature equations in §4. In §5, we seek travelling waves solutions to the nonlinear system and introduce a numerical scheme to determine the nonlinear temporal evolution of the linear wave profiles calculated in §2 using a Crank-Nicolson scheme.

2. Formulation

Working in Cartesian coordinates (x^*, y^*), we consider an incompressible, inviscid, two-dimensional flow between two flexible walls a mean distance a apart, in a gravity-free regime (see figure 1). The fluid has constant density ρ, and its pressure and velocity fields are denoted p^* and (u^*, v^*) respectively. The upper interface is located at $y^* = \eta^*_+(x^*, t^*)$ and the lower at $y^* = \eta^*_-(x^*, t^*)$. Outside of the channel is assumed to be a vacuum. If the flow and walls are undisturbed, the fluid is assumed to flow at a constant velocity U_r in the x^* direction, with the walls at $y^* = \pm a/2$. We are interested in long wavelength perturbations to this undisturbed state with wavelength L. The equations governing the unsteady fluid flow are the two dimensional Euler equations:

$$\frac{\partial u^*}{\partial x^*} + \frac{\partial v^*}{\partial y^*} = 0, \tag{1}$$

$$\frac{\partial u^*}{\partial t^*} + u^*\frac{\partial u^*}{\partial x^*} + v^*\frac{\partial u^*}{\partial y^*} = -\frac{1}{\rho}\frac{\partial p^*}{\partial x^*}, \tag{2}$$

$$\frac{\partial v^*}{\partial t^*} + u^*\frac{\partial v^*}{\partial x^*} + v^*\frac{\partial v^*}{\partial y^*} = -\frac{1}{\rho}\frac{\partial p^*}{\partial y^*}. \tag{3}$$

At the interface between the fluid and the flexible wall we have the kinematic conditions

$$\frac{\partial \eta^*_\pm}{\partial t^*} + u^*_\pm\frac{\partial \eta^*_\pm}{\partial x^*} = v^*_\pm \tag{4}$$

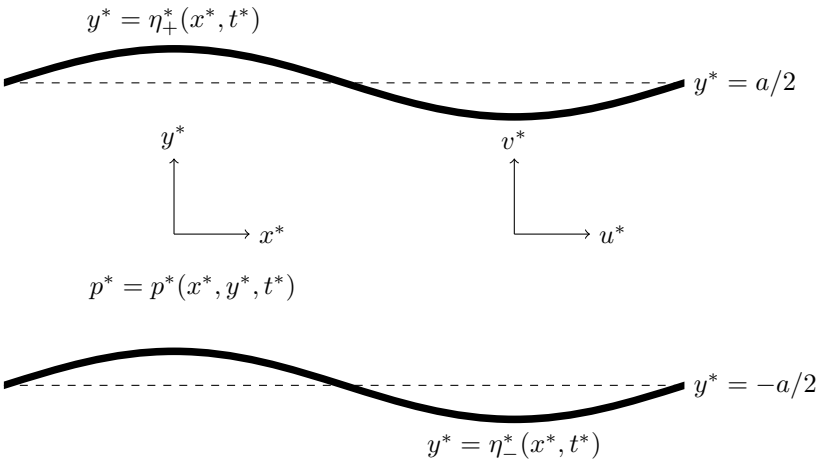

Figure 1: Dimensional problem setup.

where the subscript denotes values at the interface $y^* = \eta_\pm^*$. For the dynamic condition at the walls, Cosserat theory of hyperelastic shells satisfying Kirchhoff's hypothesis gives the pressure as

$$p_\pm^* = \pm D^* \left(\frac{\partial^2 \kappa_\pm^*}{\partial {s^*}^2} + \frac{{\kappa_\pm^*}^3}{2} \right), \tag{5}$$

where D^* is the bending stiffness, $\kappa_\pm^*$ is the curvature of the interface and $s_\pm^*$ denotes the arc length (see Plotnikov and Toland, 2011, Blyth et al., 2011). When written in terms of $\eta_\pm^*$ and x^* this becomes

$$p_\pm^* = \pm D^* \left[f_\pm^* \frac{\partial}{\partial x^*} \left(f_\pm^* \frac{\partial}{\partial x^*} \left(f_\pm^{*3} \frac{\partial^2 \eta_\pm^*}{\partial {x^*}^2} \right) \right) + \frac{1}{2} \left(f_\pm^{*3} \frac{\partial^2 \eta_\pm^*}{\partial {x^*}^2} \right)^3 \right], \tag{6}$$

with

$$f_\pm^* = \left[1 + \left(\frac{\partial \eta_\pm^*}{\partial x^*} \right)^2 \right]^{-\frac{1}{2}}. \tag{7}$$

Since there is no wall inertia in our model, the governing equations (1)–(6) are invariant under the Galilean transformation $x \mapsto x - U_r t$, $u \mapsto u - U_r$. Without loss of generality, we may therefore take $U_r = 0$ and assume there is zero mean axial flow. Solutions with a non-zero axial flux can be recovered by applying a suitable Galilean transformation.

Assuming that the fluid layer is thin compared to the wavelength of the disturbance, we follow the derivation of Mehring and Sirignano (1999) who investigated a related problem for liquid sheets. We first define the centreline $\hat{\eta}^*$ and thickness η^* by

$$\hat{\eta}^*(x^*, t^*) = \frac{\eta_+^* + \eta_-^*}{2}, \qquad \eta^*(x^*, t^*) = \eta_+^* - \eta_-^*. \tag{8}$$

The dependant variables are then expanded in powers of $y^* - \hat{\eta}^*$ as

$$u^* = u_0^*(x^*, t^*) + u_1^*(x^*, t^*)[y^* - \hat{\eta}^*] + u_2^*(x^*, t^*)[y^* - \hat{\eta}^*]^2 + \ldots, \tag{9}$$

$$v^* = v_0^*(x^*, t^*) + v_1^*(x^*, t^*)[y^* - \hat{\eta}^*] + v_2^*(x^*, t^*)[y^* - \hat{\eta}^*]^2 + \ldots, \tag{10}$$

$$p^* = p_0^*(x^*, t^*) + p_1^*(x^*, t^*)[y^* - \hat{\eta}^*] + p_2^*(x^*, t^*)[y^* - \hat{\eta}^*]^2 + \ldots. \tag{11}$$

We insert these expansions into the governing equations and boundary conditions, and consider only the lowest order in $y^*-\hat{\eta}^*$. This simplified approach removes the possibility of various hydrodynamic instabilities allowing us to focus on the fluid-structure interaction.

The resulting equations are, after some manipulation,

$$\frac{\partial \eta^*}{\partial t^*} + u_0^* \frac{\partial \eta^*}{\partial x^*} + \eta^* \frac{\partial u_0^*}{\partial x^*} = 0, \tag{12}$$

$$\frac{\partial u_0^*}{\partial t^*} + u_0^* \frac{\partial u_0^*}{\partial x^*} + \frac{u_1^{*2}\eta^*}{4} \frac{\partial \eta^*}{\partial x^*} = -\frac{1}{2\rho} \frac{\partial}{\partial x^*} \left(p_+^* + p_-^*\right) + \frac{1}{\rho \eta^*} \frac{\partial \hat{\eta}^*}{\partial x^*} \left(p_+^* - p_-^*\right) \tag{13}$$

$$\frac{\partial \hat{\eta}^*}{\partial t^*} + u_0^* \frac{\partial \hat{\eta}^*}{\partial x^*} + \frac{u_1^* \eta^*}{4} \frac{\partial \eta^*}{\partial x^*} = v_0^* \tag{14}$$

$$\frac{\partial v_0^*}{\partial t^*} + u_0^* \frac{\partial v_0^*}{\partial x^*} + \frac{v_1^* u_1^* \eta^*}{4} \frac{\partial \eta^*}{\partial x^*} = -\frac{1}{\rho \eta^*} \left(p_+^* - p_-^*\right) \tag{15}$$

To close the model we assume that $u_1^* \eta^* \ll u_0^*$ and $v_1^* \eta^* \ll v_0^*$, therefore the last term of the left hand side of (13)–(15) can be neglected. This should be fine as long as the thickness and centreline are slowly varying, i.e. $\partial \eta^*/\partial x^*$ and $\partial \hat{\eta}^*/\partial x^*$ are much less than one. Similar equations can be obtained by an integral formulation or through the use of variational methods (see Ramos (2003) for example).

We introduce non-dimensional quantities, and depart from Mehring and Sirignano (1999) by using two length scales, one each for the axial and transverse lengths. Our axial length scale is the wavelength L, and our transverse length scale is the channel width a. We denote the aspect ratio $\delta = a/L$, and assume $\delta \ll 1$. We use a pressure scale of D^*/L^3 based on the dynamic boundary condition. For the axial velocity scale, we use $U = \sqrt{D^*/2\rho L^3}$ from an inertia–pressure balance in (2). Natural time and transverse velocity scale then follow as U/L and δU. We therefore introduce the dimensionless variables

$$x = \frac{x^*}{L}, \quad t = \frac{U t^*}{L}, \quad \eta = \frac{\eta^*}{a}, \quad \hat{\eta} = \frac{\hat{\eta}^*}{a}, \quad u = \frac{u_0^*}{U}, \quad v = \frac{v_0^*}{\delta U}, \quad p_\pm = \frac{L^3 p_\pm^*}{D^*}, \quad s_\pm = \frac{s_\pm^*}{L}, \quad \kappa_\pm = \frac{L \kappa_\pm^*}{\delta}. \tag{16}$$

The final equations governing the system are found to be

$$\frac{\partial \eta}{\partial t} + \frac{\partial}{\partial x} (u\eta) = 0, \tag{17}$$

$$\frac{\partial u}{\partial t} + u \frac{\partial u}{\partial x} = -\left[\frac{\partial}{\partial x} (p_+ + p_-) - \frac{2}{\eta} \frac{\partial \hat{\eta}}{\partial x} (p_+ - p_-)\right], \tag{18}$$

$$\frac{\partial \hat{\eta}}{\partial t} + u \frac{\partial \hat{\eta}}{\partial x} = v, \tag{19}$$

$$\frac{\partial v}{\partial t} + u \frac{\partial v}{\partial x} = -\frac{2}{\delta^2 \eta} (p_+ - p_-), \tag{20}$$

where

$$p_\pm = \pm\delta \left(\frac{\partial^2 \kappa_\pm}{\partial s^2} + \frac{\delta^2}{2} \kappa_\pm^3\right) \tag{21}$$

$$\begin{aligned} &= \pm\delta f_\pm^5 \frac{\partial^4}{\partial x^4} \left(\hat{\eta} \pm \frac{\eta}{2}\right) \\ &\quad \mp \delta^3 f_\pm^7 \left[10 \frac{\partial^3}{\partial x^3} \left(\hat{\eta} \pm \frac{\eta}{2}\right) \frac{\partial^2}{\partial x^2} \left(\hat{\eta} \pm \frac{\eta}{2}\right) \frac{\partial}{\partial x} \left(\hat{\eta} \pm \frac{\eta}{2}\right) + 3 \left(\frac{\partial^2}{\partial x^2} \left(\hat{\eta} \pm \frac{\eta}{2}\right)\right)^3\right] \\ &\quad \pm \delta^3 f_\pm^9 \left[\frac{1}{2} \left(\frac{\partial^2}{\partial x^2} \left(\hat{\eta} \pm \frac{\eta}{2}\right)\right)^3 + 18\delta^2 \left(\frac{\partial^2}{\partial x^2} \left(\hat{\eta} \pm \frac{\eta}{2}\right)\right)^3 \left(\frac{\partial}{\partial x} \left(\hat{\eta} \pm \frac{\eta}{2}\right)\right)^2\right], \end{aligned} \tag{22}$$

and

$$f_\pm = \left[1 + \delta^2 \left(\frac{\partial}{\partial x} \left(\hat{\eta} \pm \frac{\eta}{2}\right)\right)^2\right]^{-\frac{1}{2}}. \tag{23}$$

Equations (17)–(20) are fully coupled, highly nonlinear equations and will be referred to as the 'full curvature system'. After the nondimensionalisation a factor of δ^{-2} remains in (20), this is an inevitable consequence of two distinct timescales in the system for symmetric and antisymmetric modes (see §3). Whichever mode is being considered, (17)–(23) contain all the leading order terms. We will consider the solution to this system numerically but to make further analytical progress we additionally consider two simplified systems.

Firstly, retaining only the linear terms in η and $\hat{\eta}$ in the expressions (22) and (23) for $p_{\pm}$, we obtain the 'linearised curvature system', which is governed by

$$\frac{\partial \eta}{\partial t} + \frac{\partial}{\partial x}(u\eta) = 0, \tag{24}$$

$$\frac{\partial u}{\partial t} + u\frac{\partial u}{\partial x} = -\delta\frac{\partial^5 \eta}{\partial x^5} + \frac{4\delta}{\eta}\frac{\partial \hat{\eta}}{\partial x}\frac{\partial^4 \hat{\eta}}{\partial x^4}, \tag{25}$$

$$\frac{\partial \hat{\eta}}{\partial t} + u\frac{\partial \hat{\eta}}{\partial x} = v, \tag{26}$$

$$\frac{\partial v}{\partial t} + u\frac{\partial v}{\partial x} = -\frac{4}{\delta\eta}\frac{\partial^4 \hat{\eta}}{\partial x^4}. \tag{27}$$

Secondly, we consider a full linearisation of (17)–(20) about the undisturbed state. Writing $\eta = 1 + \eta'$, $u = u'$, $\hat{\eta} = \hat{\eta}'$, $v = v'$ and neglecting terms that are quadratic in the primed variables we obtain

$$\frac{\partial \eta'}{\partial t} + \frac{\partial u'}{\partial x} = 0, \tag{28}$$

$$\frac{\partial u'}{\partial t} = -\delta\frac{\partial^5 \eta'}{\partial x^5} \tag{29}$$

$$\frac{\partial \hat{\eta}'}{\partial t} = v', \tag{30}$$

$$\frac{\partial v'}{\partial t} = -\frac{4}{\delta}\frac{\partial^4 \hat{\eta}'}{\partial x^4}. \tag{31}$$

This will be referred to as the 'fully linear system'. There is a full decoupling of equations (28) and (29) for u' and η' from (30) and (31) for v' and $\hat{\eta}'$. The first pair correspond to a symmetric mode, while the second pair correspond to an antisymmetric mode (de Langre, 2002). The symmetric mode is seen physically as the top and bottom interfaces being out of phase with $\eta_+^* = -\eta_-^*$, while the antisymmetric mode is seen as the interfaces being in phase with $\eta_+^* = \eta_-^*$.

3. Linear travelling waves

We seek the dispersion relations for the two pairs of decoupled equations in the fully linear system (28)–(31). From this we will be able to determine any travelling waves and their corresponding velocities.

Looking first at (28) and (29), which govern the symmetric mode, we eliminate the axial velocity, u', between them to find

$$\frac{\partial^2 \eta'}{\partial t^2} - \delta\frac{\partial^6 \eta'}{\partial x^6} = 0. \tag{32}$$

We now seek solutions of the form $\eta' = \eta'_0 \exp(i(kx - \omega t))$, were k is the wavenumber and ω is the frequency of the wave sought. Any general solution can be expressed as a superposition of these modes. Substituting the ansatz into (32), we find that the dispersion relation is

$$\omega = \pm k^3\sqrt{\delta}. \tag{33}$$

For symmetric travelling waves with wavelength 1, $k = 2\pi$ and the solutions to (28) and (29) may be written

$$\eta' = \varepsilon_s \cos(2\pi(x - c_s t)), \tag{34}$$

$$u' = \varepsilon_s c_s \cos(2\pi(x - c_s t)), \tag{35}$$

where

$$c_s = \omega/k = \pm 4\pi^2\sqrt{\delta}, \tag{36}$$

is the wave velocity and ε_s is the amplitude of the travelling wave.

Doing the same for (30) and (31), which govern the antisymmetric mode, we eliminate the transverse velocity, v', to find

$$\frac{\partial^2\hat{\eta}'}{\partial t^2} + \frac{4}{\delta}\frac{\partial^4\hat{\eta}'}{\partial x^4} = 0, \tag{37}$$

and the dispersion relation is found to be

$$\omega = \pm 2k^2\sqrt{\frac{1}{\delta}}. \tag{38}$$

So, for antisymmetric travelling waves with wavelength 1, the solutions to (30) and (31) can be written

$$\hat{\eta}' = \varepsilon_a \cos(2\pi(x - c_a t)), \tag{39}$$

$$v' = 2\pi\varepsilon_a c_a \sin(2\pi(x - c_a t)), \tag{40}$$

where

$$c_a = \omega/k = \pm 4\pi\sqrt{\frac{1}{\delta}} \tag{41}$$

is the wave velocity and ε_a is the amplitude of the travelling wave. From the calculated wave speeds above we can determine that if $\delta > 1/\pi$ the symmetric mode wave travels faster than the antisymmetric mode, and vice versa if $\delta < 1/\pi$. However, since we have made a long wave approximation, we expect $\delta \ll 1$ and therefore the antisymmetric waves always travel much faster than the symmetric waves.

4. Travelling waves in the linearised curvature system

Periodic travelling-wave solutions are sought for the linearised-curvature equations (24)–(27). We seek solutions with wavelength 1 and speed c, giving a temporal period $T = 1/c$. We therefore look for a solution in which the velocities u, v, thickness η and centreline $\hat{\eta}$ depend only upon $Z = x - ct$, and which is periodic in Z with period 1. Upon this assumption, the governing equations become

$$\frac{\mathrm{d}}{\mathrm{d}Z}\Big((u-c)\eta\Big) = 0, \tag{42}$$

$$(u-c)\frac{\mathrm{d}u}{\mathrm{d}Z} = -\delta\frac{\mathrm{d}^5\eta}{\mathrm{d}Z^5} + \frac{4\delta}{\eta}\frac{\mathrm{d}\hat{\eta}}{\mathrm{d}Z}\frac{\mathrm{d}^4\hat{\eta}}{\mathrm{d}Z^4}, \tag{43}$$

$$(u-c)\frac{\mathrm{d}\hat{\eta}}{\mathrm{d}Z} = v, \tag{44}$$

$$(u-c)\frac{\mathrm{d}v}{\mathrm{d}Z} = -\frac{2}{\delta^2\eta}\frac{\mathrm{d}^4\hat{\eta}}{\mathrm{d}Z^4}. \tag{45}$$

Since we have assumed there is no mean axial flow, there must be no net axial flux over one time period, or equivalently

$$\int_0^T u\eta\,\mathrm{d}t = 0 \qquad \Rightarrow \qquad \int_{-1/2}^{1/2} u\eta\,\mathrm{d}Z = 0. \tag{46}$$

The periodic nature of the waves being sought also means we must have conservation of mass in a spatial period. We also remove the arbitrary transverse displacement by insisting that mean centreline displacement is zero. This leads us to the constraints

$$\int_{-1/2}^{1/2} \eta\,\mathrm{d}Z = 1 \qquad \text{and} \qquad \int_{-1/2}^{1/2} \hat{\eta}\,\mathrm{d}Z = 0, \tag{47}$$

respectively.

Integrating (42) directly we obtain $(u-c)\eta = Q$, where Q is constant and, by integrating again and imposing the constraints (46) and (47), is fixed as $Q = -c$. Hence

$$u = \frac{c(\eta - 1)}{\eta}, \tag{48}$$

which, along with (44), enables u and v to be eliminated from (43) and (45), leaving a coupled system for η and $\hat{\eta}$. It is convenient to rescale the speed c and centreline position $\hat{\eta}$ as

$$c = \frac{1}{\sqrt{\delta}}\tilde{c} \qquad \text{and} \qquad \hat{\eta} = \frac{1}{\delta}\tilde{\eta}, \tag{49}$$

with the thickness η remaining unchanged. Imposing this scaling, and using (45) to rewrite the final term in (43), yields the equations governing the travelling wave solution in the form

$$\frac{\mathrm{d}^4\tilde{\eta}}{\mathrm{d}Z^4} = -\frac{\tilde{c}^2}{4\eta}\left[\frac{\mathrm{d}^2\tilde{\eta}}{\mathrm{d}Z^2} - \frac{1}{\eta}\frac{\mathrm{d}\tilde{\eta}}{\mathrm{d}Z}\frac{\mathrm{d}\eta}{\mathrm{d}Z}\right], \tag{50}$$

$$\delta^2\frac{\mathrm{d}^5\eta}{\mathrm{d}Z^5} = \frac{\tilde{c}^2}{\eta^3}\left[\frac{\mathrm{d}\eta}{\mathrm{d}Z} - \eta\frac{\mathrm{d}\tilde{\eta}}{\mathrm{d}Z}\frac{\mathrm{d}^2\tilde{\eta}}{\mathrm{d}Z^2} + \frac{\mathrm{d}\eta}{\mathrm{d}Z}\left(\frac{\mathrm{d}\tilde{\eta}}{\mathrm{d}Z}\right)^2\right]. \tag{51}$$

4.1. Symmetric mode travelling waves

Looking for purely symmetric waves first, we set the scaled centreline $\tilde{\eta} = 0$ and integrate the resulting simplified (51) once with respect to Z. We obtain a differential equation for the thickness, η,

$$\frac{\mathrm{d}^4\eta}{\mathrm{d}Z^4} = -\frac{\tilde{c}^2}{2\delta^2}\left(\frac{1}{\eta^2} - B^2\right), \tag{52}$$

where B is a constant of integration. It is convenient to make the change of variables $\eta = Y/B$, to obtain

$$\frac{\mathrm{d}^4 Y}{\mathrm{d}Z^4} = K\left(1 - \frac{1}{Y^2}\right), \tag{53}$$

where $K = \tilde{c}^2 B^3/2\delta^2$. The value of B is set by the application of (47) to any solution, from which we obtain

$$B = \int_{-1/2}^{1/2} Y \,\mathrm{d}Z. \tag{54}$$

Without loss of generality, we assume that the maximum or minimum of Y occurs at $Z = 0$, with $Y(0) = \varepsilon$. From the symmetry of (53), Y is an even periodic function on $[-1/2, 1/2]$. We restrict ourselves to $[0, 1/2]$ and therefore have the boundary conditions

$$Y(0) = \varepsilon, \qquad Y'(0) = Y'''(0) = 0, \qquad Y'(1/2) = Y'''(1/2) = 0. \tag{55}$$

The first condition fixes the amplitude of the solution while the other four arise from the symmetry of the solution. The unknown parameter K in (53) is determined as part of the solution. We thus obtain the wave speed $\tilde{c}$ in terms of the maximum or minimum amplitude ε.

The system (53) and (55) is solved numerically using the built-in MATLAB function `bvp4c`. As an initial guess for $Y(Z)$ and K we use the solution to the linearised form of (53):

$$Y = 1 - (1-\varepsilon)\cos(2\pi Z), \qquad K = 8\pi^4. \tag{56}$$

Once a solution is found, the trapezium rule is used to integrate (54) to find B, and hence η and $\tilde{c}$ can be recovered. Finally, the axial velocity, u, is found using (48). Some sample solutions for different values of ε are shown in figures 2–4.

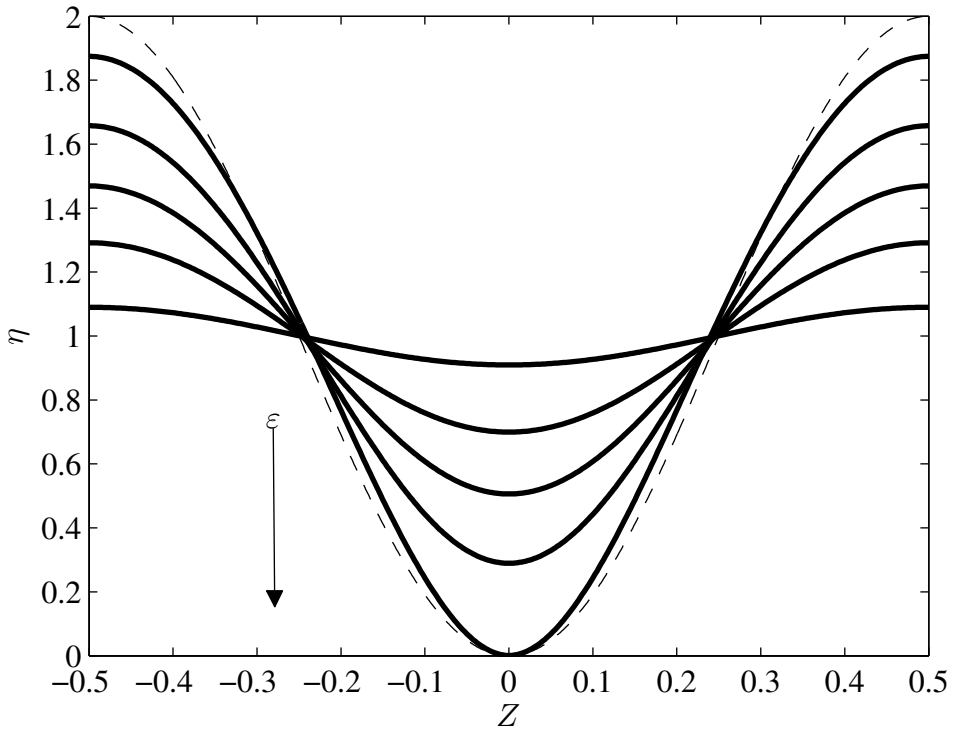

Figure 2: A selection of thickness profiles, η, for travelling waves given by (53) for $\varepsilon = 0.91, 0.75, 0.62, 0.48, 0.03$. The dashed line is $1 - \cos(2\pi Z)$ to illustrate the nonlinear effects.

In figure 2, we see that the sinusoidal shape of the travelling wave profiles found in the fully linear system given by (34) remains, however there is a flattening at the top and a sharpening at the bottom of the solution curves from the nonlinear terms. The equivalent profiles for u are shown in figure 3, where we see a strong nonlinear response as $\varepsilon \to 0$. Fluid flows in the negative x-direction at the narrowing of the channel for a wave moving in the positive x-direction, so fluid is forced from in front of the wave to behind it. As $\varepsilon \to 0$ we also see the fluid velocity descending to 0 away from the trough, this arises from the wave velocity $\tilde{c}$ being close to zero.

The relationship between the perturbation amplitude and the velocity of the travelling wave is shown in figure 4. For a given velocity, the same wave will be found twice with two different amplitudes corresponding to a translation of half a wavelength. In the limit $\varepsilon/B \to 1$, we have $\tilde{c}/\delta \to 4\pi^2$, the fixed velocity found for solutions of any amplitude in the fully linear case. In the limit $\varepsilon \to 0$, it is found that $\tilde{c} \to 0$, as the constriction prevents fluid flow back through the minimum gap.

An asymptotic analysis was performed on (53)–(55) in the limit $\varepsilon \to 0$, the details of which are included in appendix A. A composite solution was also constructed. The numerical and asymptotic results are compared in figure 5. Figure 5(a) shows the point of largest deflection, which occurs at $Z = 1/2$. The asymptotic solution remains accurate up to initial amplitudes of $\varepsilon \approx 0.1$. Similarly, figure 5(b) shows that the asymptotic solution for the unscaled velocity, K of the travelling waves remains accurate up to a similar value of ε. For an initial amplitude of $\varepsilon = 0.03$ the numerical solution is indistinguishable from the asymptotic solution (as shown in figure 5(c)), while when $\varepsilon = 0.2$ the asymptotic solution is still reasonable but it is starting to diverge from the numerical solution (see figure 5(d)). The asymptotic results for the speed–amplitude relationship are also shown in figure 4. The lower curve fits the numerical data much better because the asymptotic solution has greater accuracy there; the error in the lower line is $\mathcal{O}(\varepsilon^4)$ while in the upper line it is $\mathcal{O}(\varepsilon^8)$.

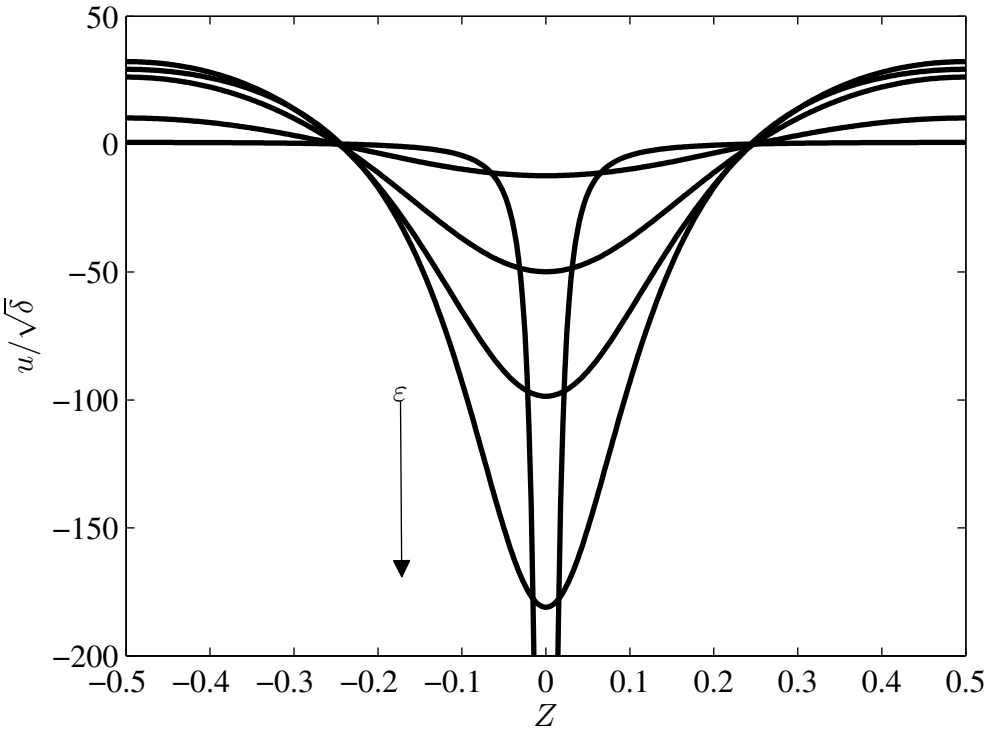

Figure 3: A selection of velocity profiles from (48), corresponding to the thickness profiles shown in figure 2. The trough of the largest wave descends to −1196.8 but has been truncated here to better illustrate the shape of the other curves.

4.2. Mixed-mode travelling waves

We now consider solutions to (50) and (51), subject to (47), in which both the channel thickness η and centreline $\tilde{\eta}$ are perturbed. In this case, we are unable to make any further analytic progress, so resort to solving the system numerically.

We observe that the equations are invariant under the transformation $Z \mapsto -Z$ and also under $\tilde{\eta} \mapsto -\tilde{\eta}$, and so expect solutions which have these symmetries. In particular, we seek solutions in which $\tilde{\eta}$ is periodic with period 1, and is either an odd or even function of Z. The form of the coupling in (51) means that η is then an even periodic function of Z with period $\frac{1}{2}$. We can therefore restrict the domain to $Z \in (0, \frac{1}{4})$, with the remainder of each solution reconstructed by symmetry. Solutions in which $\tilde{\eta}$ is odd, are simply translations of an even-$\tilde{\eta}$ solution by $\frac{1}{4}$ in Z, so these do not have to be considered separately.

Equations (50) and (51) are recast as a set of 9 first-order equations in the obvious way. From the symmetries assumed above, the boundary conditions are

$$\eta'(0) = \eta'''(0) = \tilde{\eta}'(0) = \tilde{\eta}'''(0) = 0\,, \qquad \eta'(\tfrac{1}{4}) = \eta'''(\tfrac{1}{4}) = \tilde{\eta}'(\tfrac{1}{4}) = \tilde{\eta}'''(\tfrac{1}{4}) = 0\,. \tag{57}$$

The constraint (47b) on $\tilde{\eta}$ is automatically satisfied by the symmetries assumed. The constraint (47a) on η is handled as above by introducing the incremental volume $V(Z)$ as in (63). The additional equation and boundary conditions are thus

$$\frac{\mathrm{d}V}{\mathrm{d}Z} = \eta\,; \qquad V(0) = 0\,, \qquad V(\tfrac{1}{4}) = \tfrac{1}{4}\,. \tag{58}$$

We therefore have a 10th-order system with 10 boundary conditions and one unknown parameter $\tilde{c}$. For the final condition, we can either choose $\tilde{c}$ or set the amplitude of the wave via one of $\eta(0)$ or $\tilde{\eta}(0)$. Solutions can then be found using standard shooting or discretization techniques.

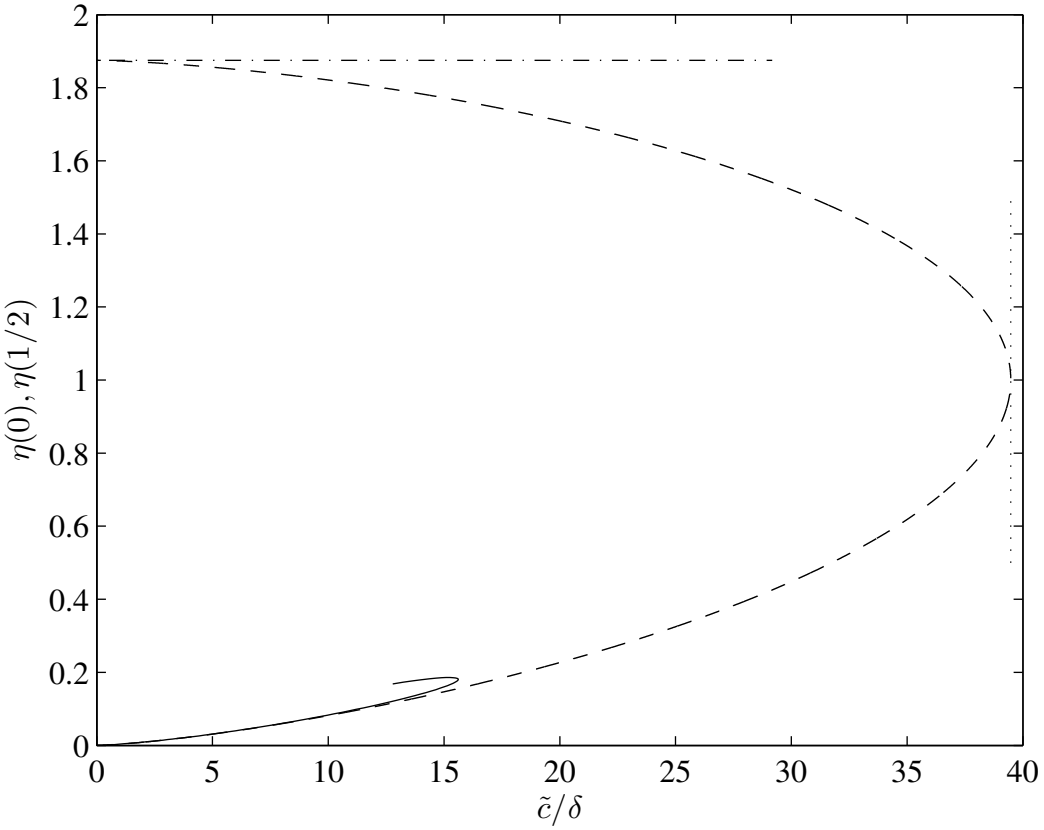

Figure 4: The velocity $\tilde{c}$ of the travelling wave as a function of the maximum or minimum displacements $\eta(0)$ and $\eta(1/2)$. The dashed line is the numerical results, the dotted line is the linear wave speed (36), then the asymptotic results are given by the solid line which is $\eta(0)$ against $\tilde{c}$ from (98) and (97) and the dot-dashed line which is $\eta(1/2)$ against $\tilde{c}$ from (99) and (97).

The various branches of solutions that we found are illustrated in figure 6, and example wall profiles are shown in figure 7. For each δ, the previous branch of symmetric solutions, in which $\tilde{\eta} \equiv 0$, still exists. (However these solutions are now forced to have period $\frac{1}{2}$ rather than 1, so are rescaled versions of those found in §4.1.) The period-$\frac{1}{2}$ symmetric branch has a maximum propagation speed of $\tilde{c}/\delta = 16\pi^2 \approx 158$, when $\eta(0) = 1$.

For each δ we find at least one additional branch of mixed-mode solutions in which $\tilde{\eta}$ is non-zero. One branch always emanates from the linear antisymmetric solution found in §3, and so has $\eta(0) - 1 = \tilde{\eta}(0) = 0$ at $\tilde{c} = 4\pi$. For some δ, a second mixed-mode branch bifurcates from the symmetric branch. There are two critical values of δ, separating different solution branch behaviour: $\delta_c = 1/(4\pi) \approx 0.0796$ and $\delta_t \approx 0.0775$.

For $\delta > \delta_c$, the solutions in the branch from the linear antisymmetric solution have lower speeds $\tilde{c} < 4\pi$. As the amplitude $\eta(0) - 1$ of the thickness increases, the amplitude $\tilde{\eta}$ of the centreline first increases and then decreases back to zero as the branch merges into the symmetric solution branch. There is also an additional branch of solutions which branches off the symmetric solution branch at a speed $\tilde{c} > 4\pi$. On this branch $\tilde{\eta}(0)$ and $\tilde{c}$ initially increase, and then decrease. The branch ends as $\tilde{\eta}(0) \to 0$ on the period-$\frac{1}{4}$ symmetric-mode branch.

At $\delta = \delta_c$, both of these mixed-mode branches start from $\eta(0) - 1 = \tilde{\eta} = 0$, $\tilde{c} = 16\pi^2\delta$, but otherwise their behaviour is the same.

For $\delta < \delta_c$, the mixed-mode branch starting from the antisymmetric linear solution at $\tilde{c} = 4\pi$ now has

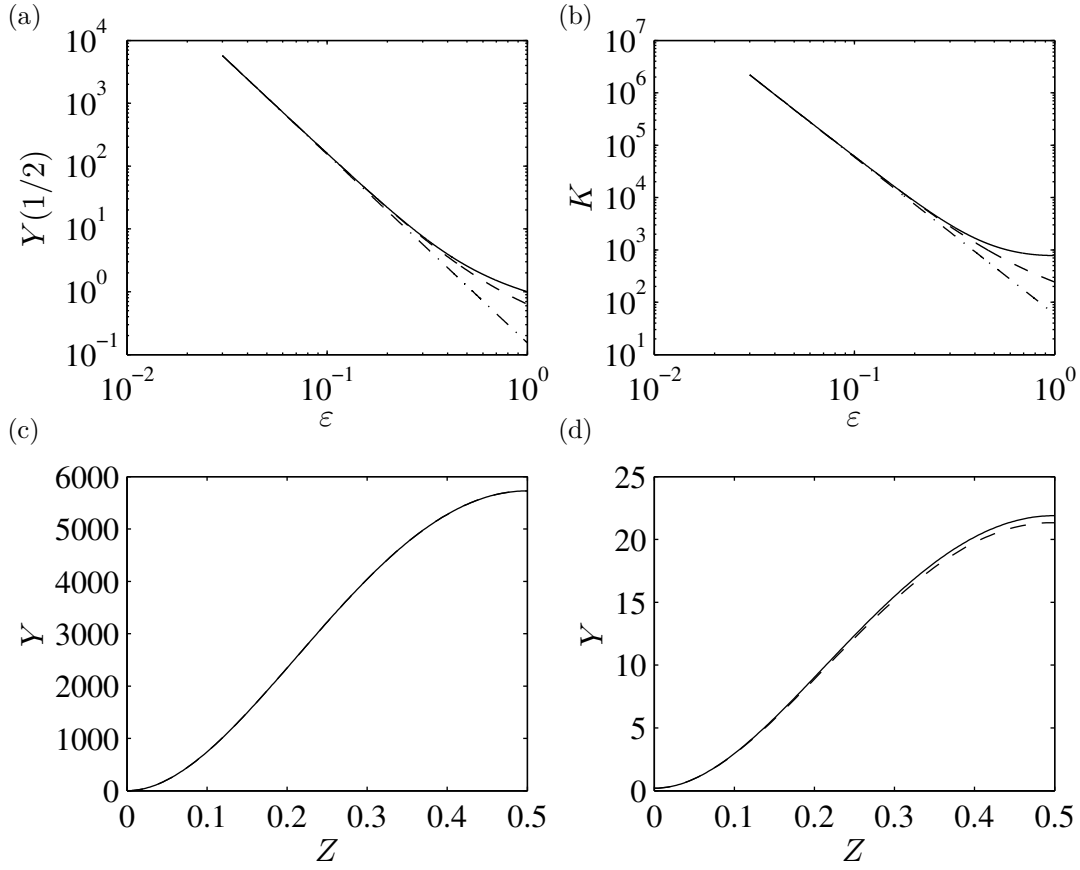

Figure 5: A comparison of the numerical results for symmetric travelling-wave solutions of the linearised curvature system (53)–(55), with the asymptotic analysis of Appendix A for $\varepsilon \ll 1$. (a) The maximum thickness perturbation $Y(1/2)$ against ε. (b) The scaled wave speed K against ε. (c) and (d) The thickness perturbation for $\varepsilon = 0.03$ and $\varepsilon = 0.2$ respectively. In all cases, the numerical results are shown with solid lines, leading-order asymptotic results with dot-dashed lines and the first order corrections with dashed lines.

speeds $\tilde{c} > 4\pi$ initially, and then loops back to the period-$\frac{1}{4}$ symmetric-mode branch (like the second branch for $\delta > \delta_c$).

When $\delta_c > \delta > \delta_t$ another mixed-mode branch exists between two points on the period-$\frac{1}{2}$ symmetric branch with $\tilde{c} < 4\pi$. These two points merge when $\delta = \delta_t$, and this other branch no longer exists for $\delta < \delta_t$.

Mixed-mode solutions with sub-linear speeds ($\tilde{c} < 4\pi$) are generally thicker ($\eta > 1$) at the extremal values of centreline displacement $\tilde{\eta}$ (figure 7(a)), while those with super-linear speeds ($\tilde{c} > 4\pi$) are generally thinner ($\eta < 1$) at the extremal values of $\tilde{\eta}$ (figure 7(b),(d)). Solutions close to the bifurcation with period-$\frac{1}{4}$ symmetric branch have a definite 4-cycles-per-period character in the thickness η, but the centreline displacement still has just one cycle (figure 7(c)).

5. Nonlinear waves

5.1. Symmetric mode travelling waves

To seek travelling wave solutions to the symmetric mode of the nonlinear system we have to use a different formulation to the one used for the linearised curvature system as we are unable to make the change of variables $\eta = Y/B$ to eliminate the constant of integration B.

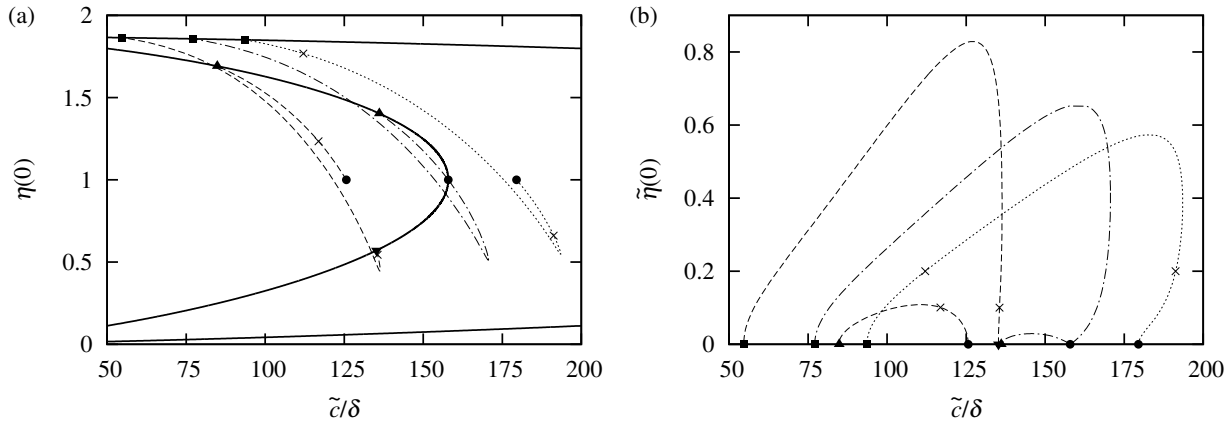

Figure 6: The branches of periodic travelling-wave solutions to (50) and (51) with period 1. The lines show mixed-mode solutions for $\delta = 0.1$ (dashed), $\delta = 1/(4\pi)$ (dot-dashed) and $\delta = 0.07$ (dotted). Also shown are the corresponding symmetric-mode branches (continuous lines) with spatial periods $\frac{1}{2}$ and $\frac{1}{4}$, which each collapse to a single curve for all δ. The various symbols indicate points where the antisymmetric amplitude $\hat{\eta}$ tends to zero, when either η tends to zero too (circles), the branch merges with the period-$\frac{1}{2}$ symmetric branch (triangles), or the branch merges with the period-$\frac{1}{4}$ symmetric branch (squares). The small crosses indicate the locations of the solutions shown below in figure 7.

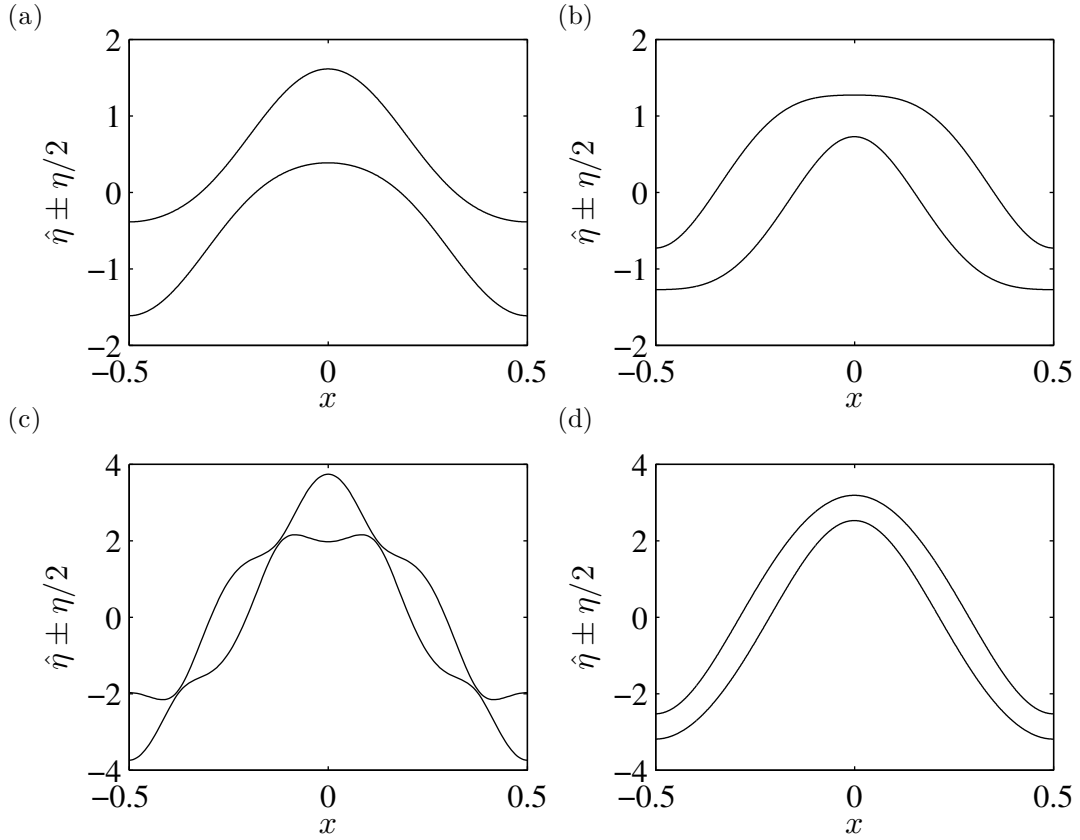

Figure 7: The deformed wall positions for four mixed-mode travelling wave solutions of (50) and (51). (a) $\delta = 0.1$, $\tilde{\eta}(0) = 0.1$, $\tilde{c} = 11.7$, (b) $\delta = 0.1$, $\tilde{\eta}(0) = 0.1$, $\tilde{c} = 13.6$, (c) $\delta = 0.07$, $\tilde{\eta}(0) = 0.2$, $\tilde{c} = 7.85$, and (d) $\delta = 0.07$, $\tilde{\eta}(0) = 0.2$, $\tilde{c} = 13.4$. These parameter choices are indicated by the small crosses in figure 6 above.

We start from (17) and (18), with $\hat{\eta} = v = 0$

$$\frac{\partial \eta}{\partial t} + \frac{\partial}{\partial x}(u\eta) = 0, \tag{59}$$

$$\frac{\partial u}{\partial t} + u\frac{\partial u}{\partial x} = -\frac{\partial p}{\partial x}, \tag{60}$$

where $p = p_+ + p_-$ and $p_\pm = \delta\left(\kappa_{ss} + \delta^2\kappa^3/8\right)$ a nondimensional form of (21). For the symmetric mode, $\kappa_+ = \kappa_-$. For convenience we have introduced $\kappa = 2\kappa_\pm$, which is then related to η by

$$\kappa = \frac{\eta_{ZZ}}{\left(1 + \frac{1}{4}\delta^2\eta_Z^2\right)^{3/2}}. \tag{61}$$

The formulation proceeds in the same way as for the linearised curvature system until (52), which is replaced with

$$-\frac{c^2}{2\delta}\left(1 - \frac{1}{\eta^2}\right) + \kappa_{ss} + \frac{\delta^2\kappa^3}{8} - B = 0. \tag{62}$$

To provide a way to ensure the conservation of mass constraint (47) can be satisfied, we introduce the incremental volume

$$V(Z) = \int_0^Z \eta(Z')\,\mathrm{d}Z'. \tag{63}$$

The fifth-order system (61)–(63) is then recast as a system of first order equations in η, η_Z, κ, κ_s and V. With five equations and two parameters B and c we require seven boundary conditions. With an imposed amplitude, the symmetry conditions used before, and required volume constraint, we set

$$\begin{aligned} &\eta(0) = 1 + a, && \eta'(0) = 0, && \kappa_s(0) = 0, && V(0) = 0, \\ &&& \eta'(1/2) = 0, && \kappa_s(1/2) = 0, && V(1/2) = 1/2. \end{aligned} \tag{64}$$

This system is then solved using `bvp4c` as previously.

The wave profiles were found to be almost identical to the profiles found for the linearised curvature system. The primary consequence of the extra nonlinearity is a lowering of the speed for a travelling wave when compared to the linearised curvature system. This is illustrated in figure 8(a) for varying values of δ, while in figure 8(b) we can see how little the wave profiles vary with δ. For the velocity, the difference between the nonlinear system and the linearised curvature system is very small for $\delta = 0.1$ but becomes greater as δ increases from there.

5.2. Numerical Scheme

In general solving (17)–(20) or (24)–(27) requires a numerical approach. Here we describe our numerical scheme for solving the general initial value problem in a frame of reference moving with the background velocity U_r, before presenting a selection of our results.

We used a finite difference method to discretise the system in both space and time. Due to the high order of some of the spatial derivatives, explicit time-stepping required prohibitively small time-step sizes for convergence. We therefore used the semi-implicit Crank-Nicolson scheme (e.g. Smith, 1985). We work with a finite domain of axial length 1, and impose periodic boundary conditions at the ends.

It is convenient to use a staggered grid, with the thickness, η, and the centreline, $\hat{\eta}$, evaluated at the grid points, and the axial and transverse velocities, u and v respectively, evaluated halfway between grid points. To ensure accuracy we use a spatial grid resolution of $\Delta x = 0.0025$ and a temporal resolution of $\Delta t = 0.0001$. This was found to be sufficiently small for the time periods considered. Solutions were also checked using finer grids but this was found not to significantly change the results, whilst greatly increasing computation time.

We note that the code is unable to handle the walls of the channel touching, or $\eta = 0$, so we terminate our calculations if $\eta = 0.01$ or less at any time-step.

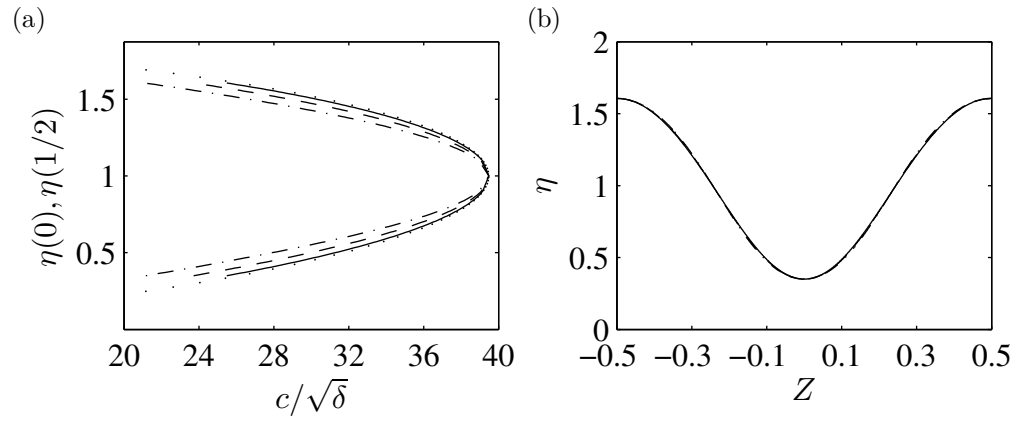

Figure 8: (a) The velocity c of the nonlinear system symmetric mode travelling waves as a function of the maximum or minimum displacements, $\eta(0)$ and $\eta(1/2)$ respectively, for varying values of δ. (b) A selection of thickness profiles for travelling solutions of the nonlinear system with $\varepsilon = 0.35$. In both cases the thin solid line is $\delta = 0.1$, the dashed line is $\delta = 0.2$ and the dot-dashed line is $\delta = 0.3$. The dotted line is the linearised curvature system velocity.

Appendix B provides further details of how the numerical scheme was validated, and figure 9 shows that the code preserves the profile of solutions to (48) and (52) when solving the linearised curvature system.

It was found that in some cases, particularly when solving the equations for large amplitude symmetric disturbances, spurious numerical oscillations occurred. To suppress this numerical noise we follow Eggers and Dupont (1994), and include an additional term in the left-hand side of the finite difference versions of (18) and (25). This takes the form of a numerical viscosity, and in derivative form it looks like

$$-\frac{\vartheta \Delta x}{\eta^2}\left(\eta^2 u u_x\right)_x, \tag{65}$$

where the subscripts denote differentiation and ϑ is an upwinding parameter. Various values of the upwinding parameter were tested but it was found that the solution was not significantly dependent on the magnitude of ϑ, therefore $\vartheta = 0.05$ was chosen following Eggers and Dupont (1994).

5.3. Symmetric waves

The effect of nonlinearity upon the propagation of waves in a symmetrically disturbed channel is investigated by comparing a linear solution, a solution of the linearised curvature system and a solution of the full curvature system. In all cases, we start with the linear solution (34) and (35) as the initial conditions for η and u at $t = 0$, with $\hat{\eta} = v = 0$. We then compare the analytical evolution of the linear solution with the numerical solutions to (24)–(25), and also (17)–(20).

Figure 10 shows the propagation of a wave with initial amplitude $\varepsilon_s = 0.7$ and $\delta = 0.1$ for one nondimensional time period $T = 0.0801$ determined by (37). It is worth noting in light of (16) the horizontal and axial length scales are different. We see that the nonlinear terms in the linearised- and full-curvature solutions reduce the velocity at which the wave propagates, as in the time taken for the linear solution to advance one wavelength, the linearised- and full-curvature solutions travel much less. This also agrees with the results from the travelling waves for the nonlinear system found previously, that the waves in that system travel slower than those in the linearised curvature system. In the nonlinear solutions, the fluid tends to group into bulges with a clear steepening and slackening of the gradient of the wall shape. Under certain circumstances this may result in a steep enough gradient to violate the slowly varying (small δ) assumption made in the formulation so care must be taken to ensure $\delta \partial \eta / \partial x < 1$.

Figure 11 shows the resultant axial velocity profiles for the perturbations. Comparing figures 10 and 11 directly we can see that the narrowing channel results in an increase in the magnitude of the velocity driving the flow backwards through the channel into the bulges.

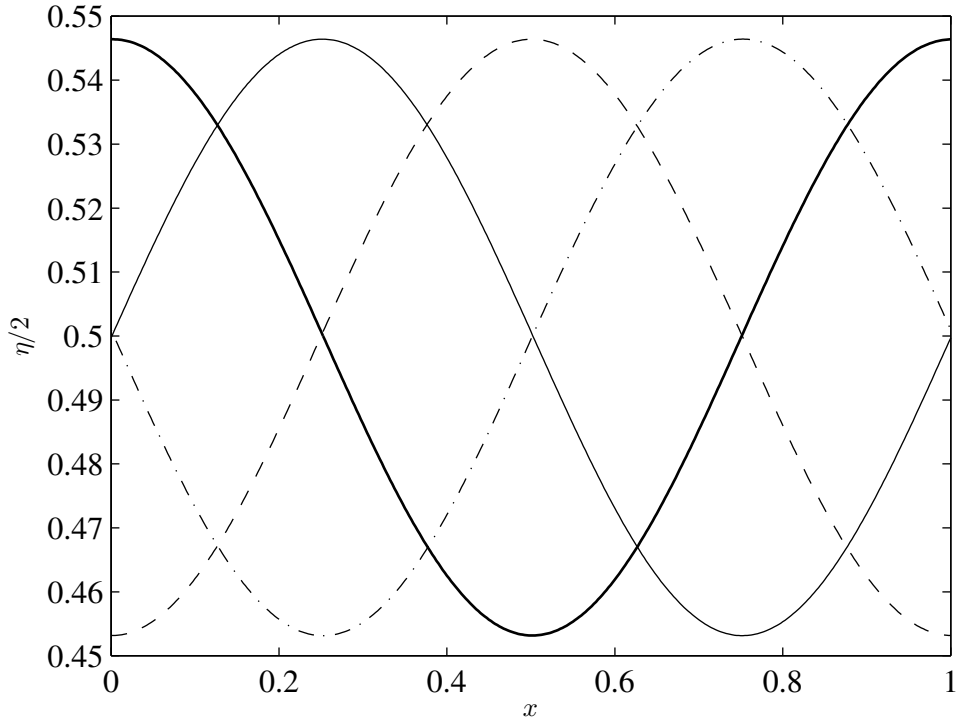

Figure 9: The evolution in time of a travelling wave from figure 2 over one time period T. Only the top interface of the channel is illustrated, with the bottom being a reflection in $\eta = 0$. The nondimensional time period is $T = 1/c = 0.08$ and the thin solid line is $t = T/4$, the dashed line is $t = T/2$, the dot-dashed line is $t = 3T/4$ and the thick solid line is $t = T$)

At this amplitude it is necessary to use the full solution as the linear and leading order solutions do not capture the full nonlinear behaviour. We note that for amplitudes of $\varepsilon_s \approx 0.3$ and below, the three solutions are virtually indistinguishable as the effect of nonlinear terms becomes negligible. For amplitudes of $\varepsilon_s \approx 0.8$ and larger, it was found that in finite time η will become small enough to halt our calculations. An example of the wall profiles and the axial velocity at the moment we stop the calculations is illustrated in figure 12.

5.4. Anti-symmetric waves

We can perform the same investigation for antisymmetric waves as we did for symmetric waves. Our three solutions are again a linear solution, a linearised curvature solution and a full curvature solution. For antisymmetric solutions the linear solution corresponds to (39), the leading-order solution to (19) and (27) with initial conditions (39), (40) and a constant thickness $\eta = 1$, and the full-curvature solution corresponds to (17)–(20) with initial conditions (39), (40), $\eta = 1$ and $u = 0$.

The propagation of the three waves for an initial amplitude $\varepsilon_a = 0.8$ is illustrated in figure 13, with $\delta = 0.1$. The coupling that is present in both the linearised and full curvature systems results in a qualitative similarity between these two results in contrast to the leading order solution. In the modes where coupling is present the channel thins on the slopes and gathers in bulges at the bends. We also see the same reduction in the wave velocity for the full-curvature solution that was present in the symmetric waves, although the effect is not as great. The antisymmetric mode can handle much larger perturbations than the symmetric mode, as a consequence the thickness is not small enough to halt the calculations until $\varepsilon_a \approx 1.25$, as illustrated in figure 14, along with the axial velocity profile. It is possible to see two spikes in the magnitude of the axial velocity profile corresponding to the two points the channel is narrowing at. It is worth noting that

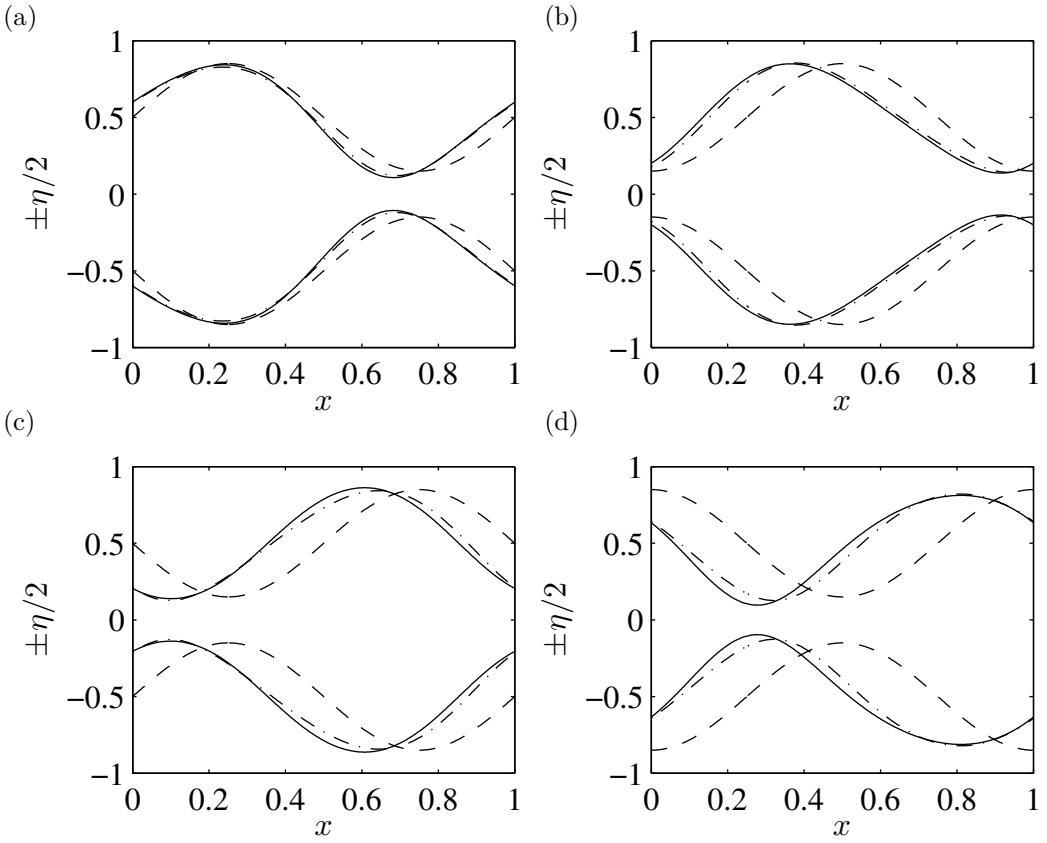

Figure 10: Propagation of waves with initial profiles given by (34) and (35) with $\varepsilon_s = 0.7$ and $\delta = 0.1$. In all cases the dashed line is the fully linearised profile, the dot-dashed line is the leading order curvature profile and the solid line is the full curvature profile. (a) $t = T/4$, (b) $t = T/2$, (c) $t = 3T/4$ and (d) $t = T$.

while both the symmetric and antisymmetric profiles illustrating the moment the calculations halt occur at the same time, this is coincidental as the calculations are stopped at different times for different initial amplitudes of the perturbations.

The difference in velocity of the waves in the symmetric mode and the antisymmetric mode has been discussed for the fully linear system and linearised-curvature system. It is illustrated for the nonlinear system in figure 15. This difference is accounted for physically by the difference in magnitude of the axial and transverse velocities required to move the fluid in the channel. To show the differing wave speeds, the symmetric and antisymmetric modes were calculated separately for the same amplitude of disturbance and parameter values, and then the deviation of the thickness and centreline from their base values were plotted for a specific point over time. In the symmetric mode we can see a higher order temporal oscillation stemming from the nonlinear terms, this is in agreement with Mehring and Sirignano (1999) who found the same oscillations arose for liquid sheets.

Figure 16 shows the evolution over one period of the thickness of disturbances to all four variables, rather than just two as illustrated previously. Even for such small perturbations, we can see that there is quite a large response when both the centreline and thickness are disturbed.

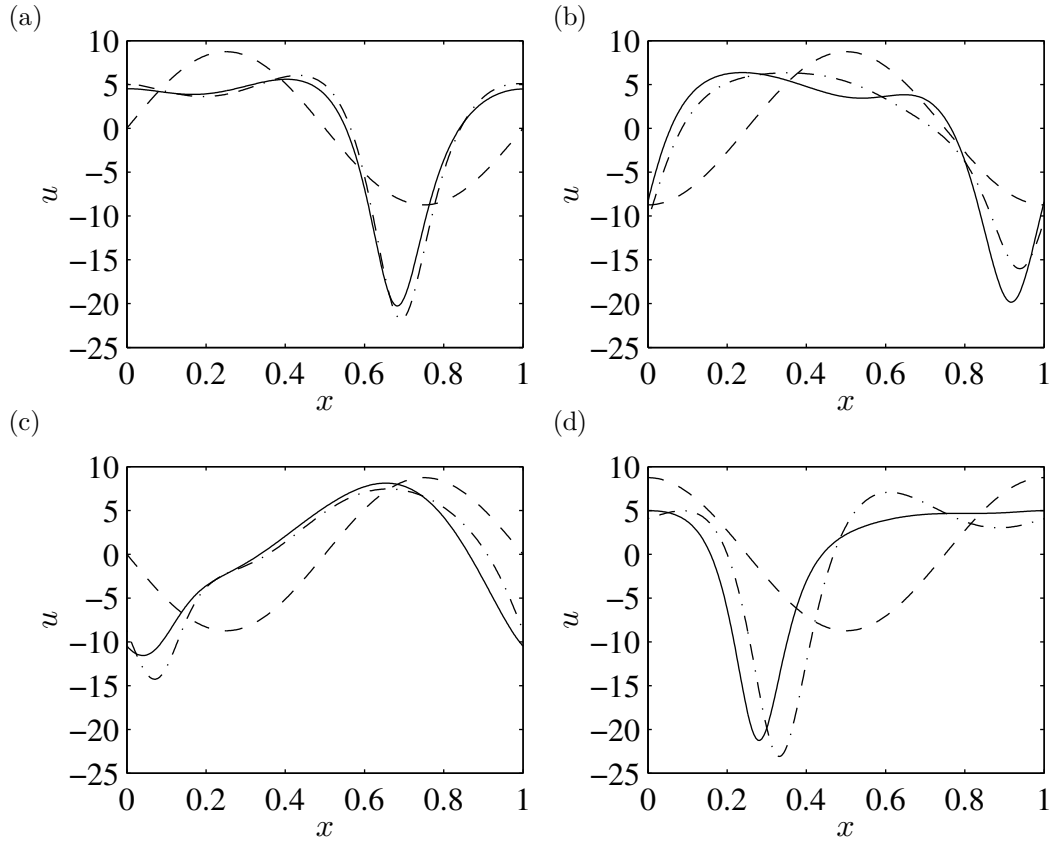

Figure 11: The axial velocity profiles associated with the wall profiles in figure 10 with $\varepsilon_s = 0.7$ and $\delta = 0.1$. In all cases the dashed line is the fully linearised profile, the dot-dashed line is the leading order curvature profile and the solid line is the full curvature profile. (a) $t = T/4$, (b) $t = T/2$, (c) $t = 3T/4$ and (d) $t = T$.

6. Discussion

We have formulated a nonlinear set of equations to describe the propagation of waves at the interface of fluid and solid in a channel with elastic sides. We also derived simplified models in the form of a linearised curvature system and a fully linearised system. For all cases we have managed to find travelling waves solutions, and in the appropriate limits have obtained good agreement between analytic, asymptotic and numerical solutions. Qualitatively the results found are similar to work done on liquid sheets. In both the symmetric and antisymmetric mode the accumulation of fluid in bulges in the channel is similar to the formation of droplets when the elastic plates are replaced by free surfaces (Mehring and Sirignano, 1999).

We considered numerical solutions of the nonlinear system to illustrate the propagation of initial disturbances. We showed that for large amplitude disturbances the curvature causes strongly nonlinear behaviour and introduces a higher order temporal oscillation on top of the main wave. Similar higher order oscillations have been observed in analogous problems for liquid sheets.

In this paper we have ignored the effects of inertia of the elastic plates to focus on the effects of nonlinearity. With inertia included linear perturbations can become unstable (see de Langre (2002)). Preliminary results for our nonlinear system with inertia included suggest that instabilities do occur and even small perturbations will lead to the channel width approaching zero. Another important effect is viscosity, where care would need to taken to resolve the expected vorticial layers that would occur at the interface between the fluid and the elastic wall. Further research is required to determine whether the opposite walls touch in

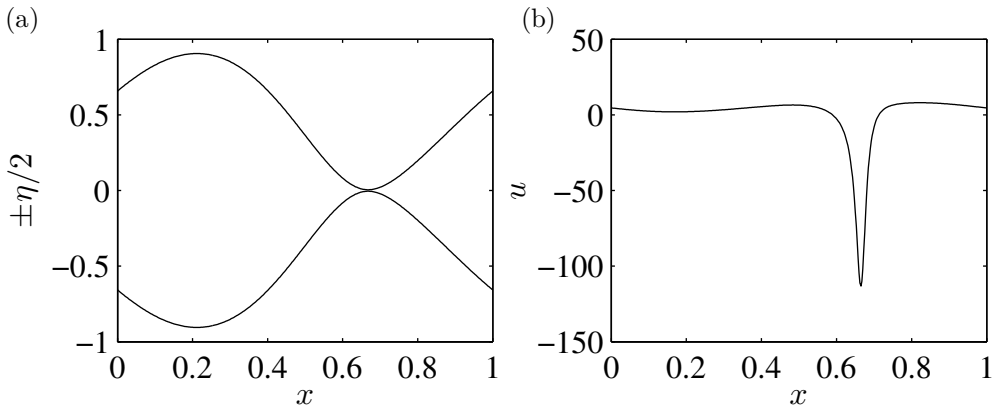

Figure 12: (a) The wall profiles as η approaches 0 for the symmetric mode. (b) The corresponding axial velocity profile. In both cases $\varepsilon_s = 0.8$, $\delta = 0.1$ and $t = 0.0241$

finite time and, if so, to model the post-contact behaviour.

7. Ackowledgements

E.I.P was supported by the EPSRC under grant EP/J019305/1. The numerical simulations presented in this paper was carried out on the High Performance Computing Cluster supported by the Research and Specialist Computing Support service at the University of East Anglia.

A. Asymptotic Analysis

In this appendix we present a matched asymptotic expansion of the solution of equation (53) subject to the boundary conditions (55) in the limit $\varepsilon \to 0$. This corresponds to the limit in which the opposite walls are almost touching. We solve for the nondimensional channel width, Y, as a function of the nondimensional axial coordinate Z, seeking a periodic solution in which $Y(0) = \varepsilon$ is the minimum width. The other parameter in the problem is a constant K, which is to be found as part of the solution.

We expect to find two asymptotic regions: an inner region close to $Z = 0$, in which $Y = \mathcal{O}(\varepsilon)$ and the right hand side of (53) is dominated by the Y^{-2} term; and an outer region in which $Z = \mathcal{O}(1)$, where Y is large and the right hand side of (53) is dominated by the constant term.

Numerical results suggest $Y''(0) \sim \varepsilon^{-3}$, giving the length-scale of the inner region as $Z = \mathcal{O}(\varepsilon^2)$; and also that $Y \sim \varepsilon^{-3}$ in the outer region, and $K \sim \varepsilon^{-3}$. The symmetries in the problem suggest an expansion in ε^2, and so we write

$$K = \varepsilon^{-3}\left(K_0 + \varepsilon^2 K_1 + \cdots\right), \tag{66}$$

where K_0, K_1 are $\mathcal{O}(1)$.

A.1. Outer Region

In the outer region Y scales like ε^{-3}, so a solution is sought of the form

$$Y = \varepsilon^{-3}\left[W_0(Z) + \varepsilon^2 W_1(Z) + \cdots\right], \tag{67}$$

Substituting (66) and (67) into (53), we obtain

$$\varepsilon^{-3}\left[\frac{\mathrm{d}^4 W_0}{\mathrm{d}Z^4} + \varepsilon^2\frac{\mathrm{d}^4 W_1}{\mathrm{d}Z^4} + \cdots\right] = \varepsilon^{-3}\left(K_0 + \varepsilon^2 K_1 + \cdots\right)\left[1 - \frac{1}{\left(\varepsilon^{-3}\left[W_0(Z) + \varepsilon^2 W_1(Z) + \cdots\right]\right)^2}\right], \tag{68}$$

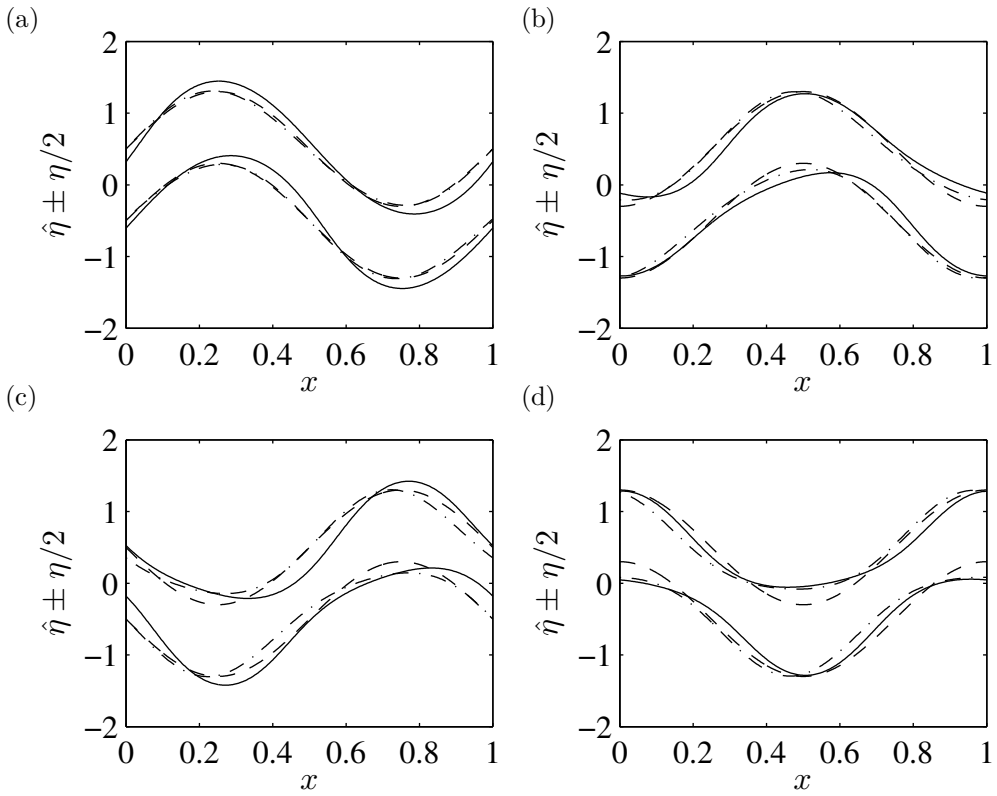

Figure 13: Propagation of waves with initial profiles given by (39) and (40) with $\varepsilon_a = 0.8$ and $\delta = 0.1$. In all cases the dashed line is the fully linearised profile, the dot-dashed line is the leading order curvature profile and the solid line is the full curvature profile. (a) $t = T/4$, (b) $t = T/2$, (c) $t = 3T/4$ and (d) $t = T$.

or alternatively,

$$\frac{\mathrm{d}^4 W_0}{\mathrm{d}Z^4} + \varepsilon^2 \frac{\mathrm{d}^4 W_1}{\mathrm{d}Z^4} + \ldots = \left(K_0 + \varepsilon^2 K_1 + \cdots\right)\left(1 + \mathcal{O}\left(\varepsilon^6\right)\right) \tag{69}$$

The boundary conditions are

$$W_0'(1/2) + \varepsilon^2 W_1'(1/2) + \ldots = 0, \qquad W_0'''(1/2) + \varepsilon^2 W_1'''(1/2) + \ldots = 0. \tag{70}$$

Writing down the leading order terms of (69) and (70), we have

$$\frac{\mathrm{d}^4 W_0}{\mathrm{d}Z^4} = K_0 \quad \text{subject to} \quad W_0'\left(1/2\right) = W_0'''\left(1/2\right) = 0. \tag{71}$$

The solution to (71) can be written as

$$W_0(Z) = \frac{K_0}{24}\left(Z - \frac{1}{2}\right)^4 + \frac{B_0}{2}\left(Z - \frac{1}{2}\right)^2 + E_0, \tag{72}$$

where B_0 and E_0 are constants of integration. The constants will be determined through matching.

Evaluating the terms at the next order we have

$$\frac{\mathrm{d}^4 W_1}{\mathrm{d}Z^4} = K_1 \quad \text{subject to} \quad W_1'\left(1/2\right) = W_1'''\left(1/2\right) = 0. \tag{73}$$

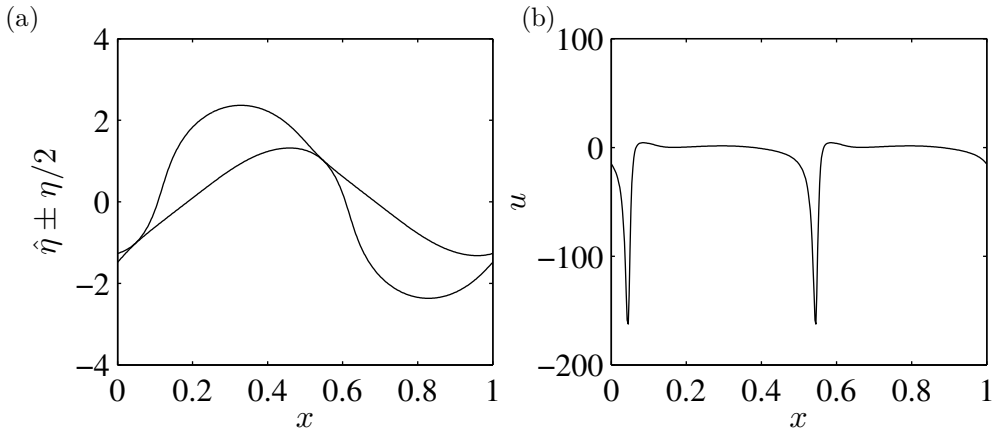

Figure 14: (a) The wall profiles as η approaches 0 for the antisymmetric mode. (b) The corresponding axial velocity profile. In both cases $\varepsilon_a = 1.25$, $\delta = 0.1$ and $t = 0.0241$

The form of the solution to (73) is the same as (72) and after application of the boundary conditions is

$$W_1(Z) = \frac{K_1}{24}\left(Z - \frac{1}{2}\right)^4 + \frac{B_1}{2}\left(Z - \frac{1}{2}\right)^2 + E_1, \tag{74}$$

with K_1, B_1 and E_1 to be determined through matching.
The outer solution with first-order correction is therefore

$$Y = \varepsilon^{-3}\left[\frac{K_0}{24}\left(Z - \frac{1}{2}\right)^4 + \frac{B_0}{2}\left(Z - \frac{1}{2}\right)^2 + E_0 + \varepsilon^2\left(\frac{K_1}{24}\left(Z - \frac{1}{2}\right)^4 + \frac{B_1}{2}\left(Z - \frac{1}{2}\right)^2 + E_1\right) + \cdots\right]. \tag{75}$$

A.2. Inner Region

For the inner solution we use the scaled coordinate $\zeta = Z/\varepsilon^2$. In this inner region, Y scales like ε, so a solution is sought in the form

$$Y = \varepsilon\left(F_0(\zeta) + \varepsilon^2 F_1(\zeta) + \varepsilon^4 F_2(\zeta) + \cdots\right). \tag{76}$$

We substitute (76) into (53) and obtain

$$\varepsilon^{-7}\frac{\mathrm{d}^4 F_0}{\mathrm{d}\zeta^4} + \varepsilon^{-5}\frac{\mathrm{d}^4 F_1}{\mathrm{d}\zeta^4} + \varepsilon^{-3}\frac{\mathrm{d}^4 F_2}{\mathrm{d}\zeta^4} + \cdots = \varepsilon^{-3}\left(K_0 + \varepsilon^2 K_1 + \cdots\right)\left(1 - \varepsilon^{-2}F_0^{-2}\left(1 + 2\varepsilon^2\frac{F_1}{F_0} + \cdots\right)\right). \tag{77}$$

or alternatively,

$$\frac{\mathrm{d}^4 F_0}{\mathrm{d}\zeta^4} + \varepsilon^2\frac{\mathrm{d}^4 F_1}{\mathrm{d}\zeta^4} + \varepsilon^4\frac{\mathrm{d}^4 F_2}{\mathrm{d}\zeta^4} + \cdots = \varepsilon^2\Big(K_0 + \varepsilon^2 K_1 + \mathcal{O}\left(\varepsilon^4\right)\Big)\left(-F_0^{-2} + \varepsilon^2\left(1 + 2\frac{F_1}{F_0^3}\right) + \mathcal{O}\left(\varepsilon^4\right)\right). \tag{78}$$

subject to

$$F_0(0) + \varepsilon^2 F_1(0) + \ldots = 1, \qquad F_0'(0) + \varepsilon^2 F_1'(0) + \ldots = 0, \qquad F_0'''(0) + \varepsilon^2 F_1'''(0) + \ldots = 0. \tag{79}$$

At leading order (78) and (79) imply

$$\frac{\mathrm{d}^4 F_0}{\mathrm{d}\zeta^4} = 0, \qquad \text{subject to} \qquad F_0(0) = 1, \quad F_0'(0) = F_0'''(0) = 0. \tag{80}$$

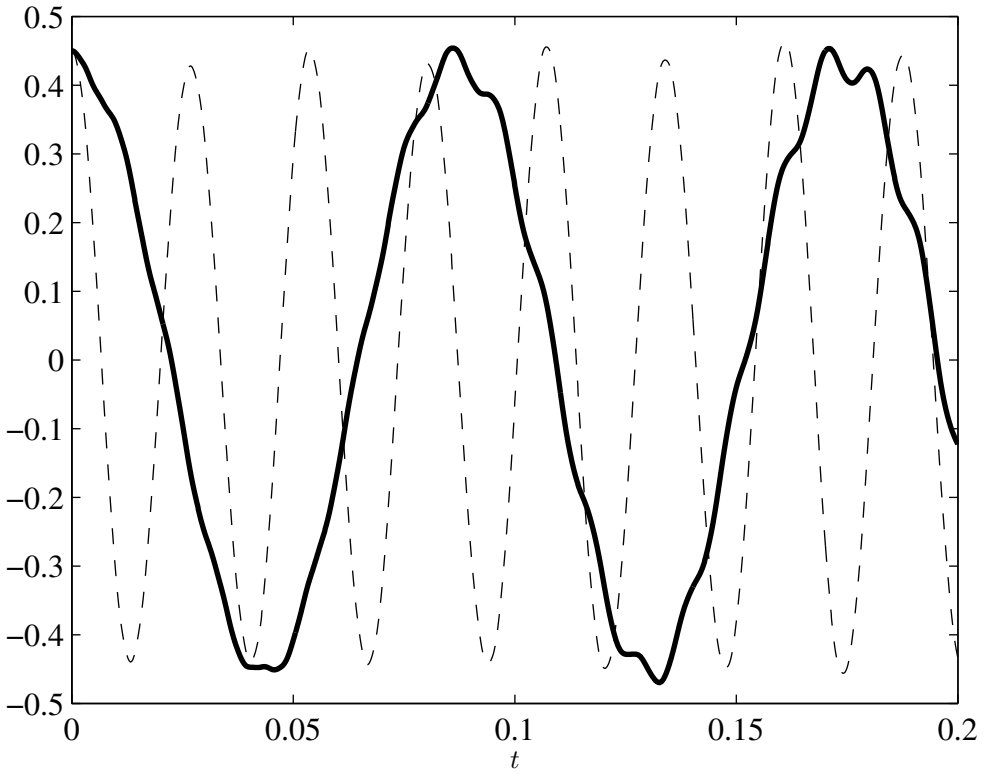

Figure 15: The deviation from the undisturbed values of the thickness with $\varepsilon_s = 0.45$ and $\delta = 1$ given by the solid line, and the centreline with $\varepsilon_a = 0.45$ and $\delta = 0.1$ given by the dashed line.

The solution to (80) is

$$F_0 = 1 + a_0^2 \zeta^2, \tag{81}$$

where the constant a_0 will be determined by matching.

At $\mathcal{O}(\varepsilon^{-2})$, (78) and (79) imply

$$\frac{\mathrm{d}^4 F_1}{\mathrm{d}\zeta^4} = -\frac{K_0}{F_0^2} \qquad \text{subject to} \qquad F_1(0) = F_1'(0) = F_1'''(0) = 0. \tag{82}$$

The solution of (82) is

$$F_1 = -\frac{K_0}{4a_0}\left[\left(\frac{\zeta^3}{3} + \frac{\zeta}{a_0^2}\right)\arctan\left(a_0^2\zeta\right) - \frac{1}{3a_0^3}\ln\left(1 + a_0^2\zeta^2\right) + \hat{\beta}_1\zeta^2\right], \tag{83}$$

where $\hat{\beta}_1$ is another constant, which can only be determined by matching.

To achieve a full matching it becomes necessary to determine some behaviour of the second-order correction, F_2, to the inner solution. At $\mathcal{O}(\varepsilon^4)$, (78) implies

$$\frac{\mathrm{d}^4 F_2}{\mathrm{d}\zeta^4} = -\frac{K_1}{F_0^2} + K_0\left(1 + 2\frac{F_1}{F_0^3}\right) \qquad \text{subject to} \qquad F_2(0) = F_2'(0) = F_2'''(0) = 0. \tag{84}$$

Writing

$$F_2 = \frac{K_0\zeta^4}{24} + \tilde{F}_2(\zeta), \tag{85}$$

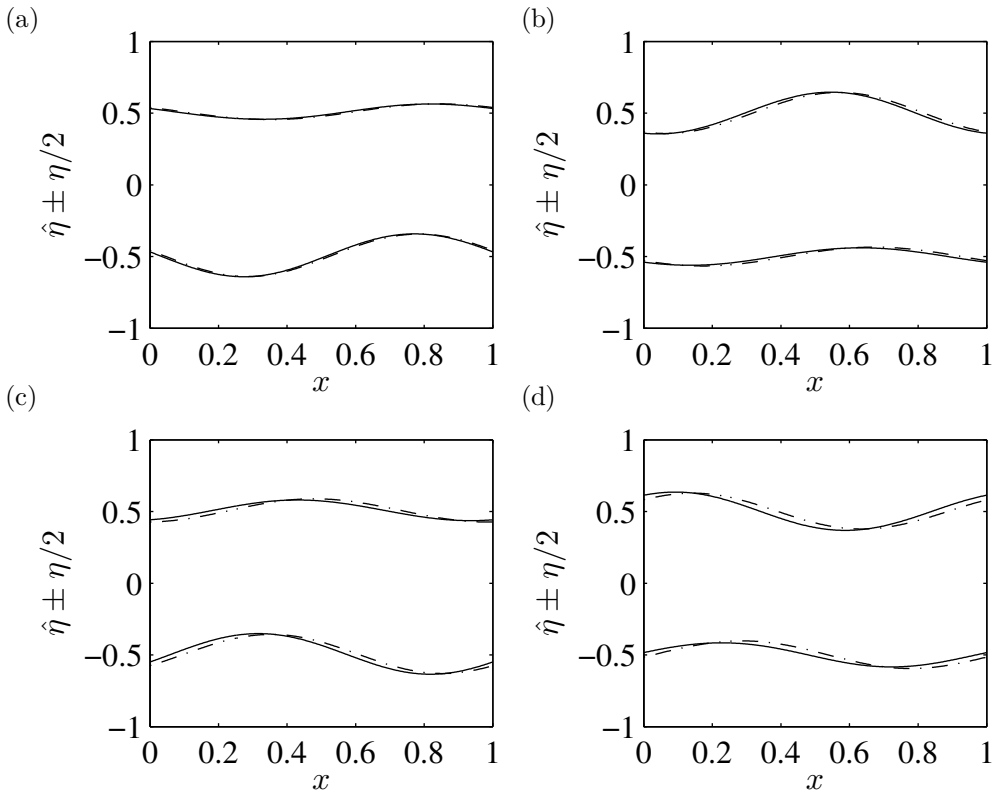

Figure 16: Propagation of waves with initial profiles given by (34), (35), (39) and (40) with $\varepsilon_a = \varepsilon_s = 0.1$ and $\delta = 0.1$. In both cases the leading order curvature profile is given by the dot-dashed line and the full curvature profile is given by the solid line. (a) $t = T/4$, (b) $t = T/2$, (c) $t = 3T/4$ and (d) $t = T$.

we see that

$$\frac{\mathrm{d}^4\tilde{F}_2}{\mathrm{d}\zeta^4} = -\frac{K_1}{F_0^2} + 2K_0\frac{F_1}{F_0^3} \qquad \text{subject to} \qquad \tilde{F}_2(0) = \tilde{F}_2'(0) = \tilde{F}_2'''(0) = 0. \tag{86}$$

In the limit $\zeta \to \infty$, $\tilde{F}_2'''' \to 0$ which implies $\tilde{F}''' \to \alpha_2$, a constant. We then have

$$\alpha_2 = \left[\tilde{F}_2'''\right]_0^\infty = \int_0^\infty \frac{\mathrm{d}^4\tilde{F}_2}{\mathrm{d}\zeta^4}\,\mathrm{d}\zeta = \left(-\frac{K_1\pi}{4a_0} - \frac{K_0^2}{6a_0^5}\left[\frac{\pi}{16}\left(7 - 3\ln(4)\right) + \frac{3\hat{\beta}_1 a_0\pi}{16}\right]\right). \tag{87}$$

The large-ζ behaviour of F_2 is thus given by $F_2 \sim K_0\zeta^4/24 + \alpha_2\zeta^3/6 + \cdots$. Similarly, it can be shown that $F_3 \sim K_1\zeta^4/24$ as $\zeta \to \infty$. We now have all the terms necessary to provide a complete matching.

The inner solution, is then given by

$$\begin{aligned} Y = \varepsilon\Bigg(1 + a_0^2\zeta^2 - \varepsilon^2\frac{K_0}{4a_0}\left[\left(\frac{\zeta^3}{3} + \frac{\zeta}{a_0^2}\right)\arctan(\zeta) - \frac{1}{3a_0^3}\ln\left(1 + a_0^2\zeta^2\right) + \hat{\beta}_1\zeta^2\right] \\ + \varepsilon^4\left[\frac{K_0}{24}\zeta^4 + \frac{1}{6}\alpha_2\zeta^3 + \cdots\right] + \varepsilon^6\left[\frac{K_1}{24}\zeta^4 + \cdots\right] + \cdots\Bigg), \end{aligned} \tag{88}$$

or, when rewritten in terms of Z,

$$Y = \varepsilon\left(1 + a_0^2\frac{Z^2}{\varepsilon^4} - \varepsilon^2\frac{K_0}{4a_0}\left[\left(\frac{Z^3}{3\varepsilon^6} + \frac{Z}{a_0^2\varepsilon^2}\right)\arctan\left(a_0\frac{Z}{\varepsilon^2}\right) - \frac{1}{3a_0^3}\ln\left(1 + a_0^2\frac{Z^2}{\varepsilon^4}\right) + \hat{\beta}_1\frac{Z^2}{\varepsilon^4}\right]\right.$$
$$\left. + \varepsilon^4\left[\frac{K_0}{24}\frac{Z^4}{\varepsilon^8} + \frac{1}{6}\alpha_2\frac{Z^3}{\varepsilon^6} + \cdots\right] + \varepsilon^6\left[\frac{K_0}{24}\frac{Z^4}{\varepsilon^8} + \cdots\right] + \cdots\right). \tag{89}$$

A.3. Matching

To perform an accurate matching it is traditional to introduce an intermediate variable, however, in this case it was possible to perform the matching in terms of the outer variable Z. Beginning with the outer solution (75), we write it in terms of ascending powers of ε

$$Y = \varepsilon^{-3}\left[\left(\frac{K_0}{384} + \frac{B_0}{8} + E_0\right) - Z\left(\frac{K_0}{48} + \frac{B_0}{2}\right) + Z^2\left(\frac{K_0}{16} + \frac{B_0}{2}\right) - Z^3\frac{K_0}{12} + Z^4\frac{K_0}{24}\right]$$
$$+ \varepsilon^{-1}\left[\left(\frac{K_1}{384} + \frac{B_1}{8} + E_1\right) - Z\left(\frac{K_1}{48} + \frac{B_1}{2}\right) + Z^2\left(\frac{K_1}{16} + \frac{B_1}{2}\right) - Z^3\frac{K_1}{12} + Z^4\frac{K_1}{24}\right] + \cdots. \tag{90}$$

For the inner solution (89), in the limit $\varepsilon \to 0$ the natural log term is negligible relative to the other terms and we replace the arctan term with the first two terms of an expansion around $Z = \infty$. Written in ascending powers of ε it becomes

$$Y = \varepsilon^{-3}\left[Z^2a_0^2 - Z^3\frac{K_0\pi}{24a_0} + Z^4\frac{K_0}{24}\right]$$
$$+ \varepsilon^{-1}\left[Z^2\left(\frac{K_0}{12a_0^2} - \frac{K_0\hat{\beta}_1}{4a_0}\right) - Z^3\frac{1}{6}\left(\frac{K_1\pi}{4a_0} + \frac{K_0^2}{6a_0^5}\left[\frac{\pi}{16}(7 - 3\ln(4)) + \frac{3\hat{\beta}_1a_0\pi}{16}\right]\right) + Z^4\frac{K_1}{24}\right] + \cdots. \tag{91}$$

Comparing coefficients of varying powers of Z in the ε^{-3} terms in (90) and (91) we obtain a set of equations for a_0, K_0, B_0 and E_0. These can be solved to find

$$a_0 = \frac{\pi}{2}, \quad K_0 = 6\pi^2, \quad B_0 = -\frac{\pi^2}{4}, \quad E_0 = \frac{\pi^2}{64}. \tag{92}$$

Comparing the coefficients in the ε^{-1} terms gives us a set of equations for $\hat{\beta}_1$, K_1, B_1 and E_1, which when solved yield

$$\hat{\beta}_1 = -\frac{2}{3\pi}(7 - 6\ln(2)), \quad K_1 = 96(4 - 3\ln(2)), \quad B_1 = 4(3\ln(2) - 4), \quad E_1 = \frac{1}{4}(4 - 3\ln(2)). \tag{93}$$

In both cases, there are five equations for only four unknowns, but the coefficients of Z^4 are already identical, reducing the number of equations by one.

A.4. Composite Solution

To calculate a composite solution, which is valid across the entire domain, we add together the inner and outer solutions and subtract off the overlapping terms. The overlapping terms are the limit of the outer solution as $Z \to 0$, or equivalently the limit of the inner solution as $\zeta \to 0$. Substitution of (92) and (93)

removes the parameters from the solution, and the composite solution is then

$$Y = \varepsilon^{-3}\left\{\frac{\pi^2}{4}\left(Z-\frac{1}{2}\right)^4 - \frac{\pi^2}{8}\left(Z-\frac{1}{2}\right)^2 + \frac{\pi^2}{64} + \varepsilon^2\left(4\left(4-3\ln(2)\right)\left(Z-\frac{1}{2}\right)^4\right.\right.$$
$$\left.\left.+2\left(3\ln(2)-4\right)\left(Z-\frac{1}{2}\right)^2 + \frac{1}{4}\left(4-3\ln(2)\right)\right)\right\} + \varepsilon\left\{1 + \frac{\pi^2 Z^2}{4\varepsilon^4}\right.$$
$$\left.-\varepsilon^2 3\pi\left[\left(\frac{Z^3}{3\varepsilon^6} + \frac{4Z}{\pi^2\varepsilon^2}\right)\arctan\left(\frac{\pi Z}{2\varepsilon^2}\right) - \frac{8}{3\pi^3}\ln\left(1+\frac{\pi^2 Z^2}{4\varepsilon^4}\right) - \frac{2}{3\pi}\left(7-3\ln(4)\right)\frac{Z^2}{\varepsilon^4}\right]\right\}$$
$$-\left\{\frac{\pi^2 Z^2}{4\varepsilon^3} - \frac{\pi^2 Z^3}{2\varepsilon^3} + \left(16-6\ln(4)\right)\frac{Z^2}{\varepsilon}\right\}. \tag{94}$$

The term in the first set of curly brackets is the outer solution, the second set contains the inner solution and the third set are the overlap terms. The second-order correction terms to the inner are omitted from the composite solution as they were not fully calculated, and only used to provide a complete matching.

A.5. Recovery of η and $\tilde{c}$

To express this solution in terms of the scaled variable η we need to compute B using (54). Taking into account the symmetries of the solution we have

$$B = 2\int_0^{1/2} Y \,\mathrm{d}Z. \tag{95}$$

Looking again at (94) we can see that the contributions from the inner solution at the two leading orders $\mathcal{O}(\varepsilon^{-3})$ and $\mathcal{O}(\varepsilon^{-1})$ are cancelled out by the terms in the overlap, so the greatest contribution from the inner solution will be $\mathcal{O}(\varepsilon)$, this takes place over the inner region of $\mathcal{O}(\varepsilon^2)$ so we would expect the contribution from the integral to be $\mathcal{O}(\varepsilon^3)$. This is negligible compared with the contribution from the outer solution. So we can rewrite (95) as

$$B = 2\varepsilon^{-3}\int_0^{1/2} W_0 + \varepsilon^2 W_1 \,\mathrm{d}Z + \mathcal{O}(\varepsilon) = \varepsilon^{-3}\left(\frac{\pi^2}{120} + 2\varepsilon^2\left(\frac{4-3\ln(2)}{15}\right) + \mathcal{O}\left(\varepsilon^4\right)\right). \tag{96}$$

Using (66) and (96) the wave-speed $\tilde{c}$ can then be expanded as

$$\tilde{c} = \sqrt{\frac{2KD}{B^3}}\delta = \frac{1440}{\pi^2}\sqrt{10}\delta\varepsilon^3\left(1 - \frac{16}{\pi^2}\varepsilon^2\left(4-3\ln(2)\right) + \mathcal{O}\left(\varepsilon^4\right)\right), \tag{97}$$

while using (96) the minimum value of η can be expanded as

$$\eta(0) = \frac{\varepsilon}{B} = \frac{120}{\pi^2}\varepsilon^4\left(1 - \frac{16}{\pi^2}\varepsilon^2\left(4-3\ln(2)\right) + \mathcal{O}\left(\varepsilon^4\right)\right). \tag{98}$$

Finally, using (75) and (96), the maximum value of η can be expanded as

$$\eta\left(1/2\right) = \frac{Y\left(1/2\right)}{B} = \frac{15}{8}\Big(1 + \mathcal{O}\left(\varepsilon^4\right)\Big). \tag{99}$$

B. Validation of the numerical scheme

In this appendix we provide details on the validation of the numerical scheme introduced in §5. In addition to standard convergence tests, we also check that the code preserves a known travelling wave, and that energy is conserved.

B.1. Convergence Tests

As a further check on the numerical schemes, we tested a variety of spatial and temporal grid resolutions. We found that for grids finer than the chosen spatial resolution $\Delta x = 0.0025$ and temporal resolution $\Delta t = 0.0001$ the accuracy was not measurably improved however computation time was greatly increased. For rougher grids some accuracy was lost, and it increased the chance of the occurrence of spurious numerical oscillations.

B.2. Preservation of known travelling waves

We used the Crank–Nicolson scheme outlined in §5 for the linearised curvature system, to propagate solutions of (48) and (52) forward for one nondimensional time period. The aim of this was to ensure that the profile of the wave was preserved, figure 9 illustrates that this was indeed the case.

B.3. Conservation of Energy

We examine the change in energy for a purely symmetric mode with axial velocity u and channel width η, in the linearised curvature system over time. If we multiply (25) by $u\eta$, rearrange the derivatives and integrate over one wavelength, then we find

$$\frac{\mathrm{d}}{\mathrm{d}t}\int_0^1 \left\{ \frac{\eta u^2}{2} + \frac{\delta}{2}\left(\frac{\partial^2 \eta}{\partial x^2}\right)^2 \right\} \mathrm{d}x + \left[\frac{\eta u^3}{2} + \delta\left(u\eta \frac{\partial^4 \eta}{\partial x^4} + \frac{\partial \eta}{\partial t}\frac{\partial^3 \eta}{\partial x^3} - \frac{\partial^2 \eta}{\partial t \partial x}\frac{\partial^2 \eta}{\partial x^2} \right) \right]_0^1 = 0, \tag{100}$$

The two terms in the integrand in (100) represent kinetic energy in the fluid and bending energy in the wall respectively. The terms contained within the square brackets represent energy fluxes with the first being the flux of kinetic energy, while the final three represent flux of bending energy. This is a conservation equation for the energy, however, all the terms in the square brackets in (100) are periodic in space and so this equation simplifies to

$$\int_0^1 \frac{\eta u^2}{2} + \frac{\delta}{2}\left(\frac{\partial^2 \eta}{\partial x^2}\right)^2 \mathrm{d}x = E_l, \tag{101}$$

where E_l is the constant energy in the system. This integral is evaluated numerically at every time step using the trapezium rule. We found that the energy varied on a scale of $\mathcal{O}\left(10^{-5}\right)$ implying the energy is conserved and therefore that the wave is neutrally stable, as we would expect an unstable wave to have an energy increase associated with it, and a decaying wave to have an energy decrease.

Similarly, we can construct an energy equation for the full-curvature system, which is

$$\frac{1}{2}\int_0^1 \eta\left(u^2 + \delta^2 v^2\right) \mathrm{d}x + \frac{1}{2}\int_0^1 \frac{\eta_+''^2}{\left(1+\eta_+'^2\right)^{5/2}} + \frac{\eta_-''^2}{\left(1+\eta_-'^2\right)^{5/2}} \mathrm{d}x = E_f, \tag{102}$$

where E_f is the constant energy in the system.

References

Blyth, M., Părău, E., Vanden-Broeck, J., 2011. Hydroelastic waves on fluid sheets. Journal of Fluid Mechanics 689, 541–551.

Eggers, J., Dupont, T.F., 1994. Drop formation in a one-dimensional approximation of the Navier–Stokes equation. Journal of Fluid Mechanics 262, 205–221.

Grotberg, J., 1994. Pulmonary flow and transport phenomena. Annual Review of Fluid Mechanics 26, 529–571.

Kim, G., Davis, D., 1995. Hydrodynamic instabilities in flat-plate-type fuel assemblies. Nuclear Engineering and Design 158, 1–17.

Korobkin, A., Părău, E.I., Vanden-Broeck, J.M., 2011. The mathematical challenges and modelling of hydroelasticity. Philosophical Transactions of the Royal Society A: Mathematical, Physical and Engineering Sciences 369, 2803–2812.

de Langre, E., 2002. Absolutely unstable waves in inviscid hydroelastic systems. Journal of Sound and Vibration 256, 299–317.

de Langre, E., Ouvrard, A.E., 1999. Absolute and convective bending instabilities in fluid-conveying pipes. Journal of Fluids and Structures 13, 663–680.

Li, X., 1993. Spatial instability of plane liquid sheets. Chemical Engineering Science 48, 2973–2981.

Mehring, C., Sirignano, W., 1999. Nonlinear capillary wave distortion and disintegration of thin planar liquid sheets. Journal of Fluid Mechanics 388, 69–113.
Michelin, S., Llewellyn Smith, S., 2009. Linear stability of coupled parallel flexible plates in an axial flow. Journal of FLuids and Structures 25, 1136–1157.
Peake, N., 2001. Nonlinear stability of a fluid-loaded elastic plate with mean flow. Journal of Fluid Mechanics 434, 101–118.
Plotnikov, P., Toland, J.F., 2011. Modelling nonlinear hydroelastic waves. Philosophical Transactions of the Royal Society A: Mathematical, Physical and Engineering Sciences 369, 2942–2956.
Ramos, J., 2003. Oscillatory dynamics of inviscid planar liquid sheets. Applied Mathematics and Computation 143, 109–144.
Schouveiler, L., Eloy, C., 2009. Coupled flutter of parallel plates. Phys. Fluids 21, 081703.
Smith, G.D., 1985. Numerical solution of partial differential equations: finite difference methods. Oxford University Press.
Squire, H., 1953. Investigation of the instability of a moving liquid film. British Journal of Applied Physics 4, 167–169.
Tang, L., 2007. The dynamics of two-dimensional cantilevered flexible plates in axial flow and a new energy-harvesting concept. PhD Thesis .
Tang, L., Païdoussis, M., 2009. The coupled dynamics of two cantilevered flexible plates in axial flow. Journal of Sound and Vibration 323, 790–801.
Walsh, C., 1995. Flutter in one-dimensional collapsible tubes. Journal of Fluids and Structures 9, 393–408.

Figure 1: Dimensional problem setup.

Figure 2: A selection of thickness profiles, η, for travelling waves given by (53) for $\varepsilon = 0.91, 0.75, 0.62, 0.48, 0.03$. The dashed line is $1 - \cos(2\pi Z)$ to illustrate the nonlinear effects.

Figure 3: A selection of velocity profiles from (48), corresponding to the thickness profiles shown in figure 2. The trough of the largest wave descends to -1196.8 but has been truncated here to better illustrate the shape of the other curves.

Figure 4: The velocity $\tilde{c}$ of the travelling wave as a function of the maximum or minimum displacements $\eta(0)$ and $\eta(1/2)$. The dashed line is the numerical results, the dotted line is the linear wave speed (36), then the asymptotic results are given by the solid line which is $\eta(0)$ against $\tilde{c}$ from (98) and (97) and the dot-dashed line which is $\eta(1/2)$ against $\tilde{c}$ from (99) and (97).

Figure 5: A comparison of the numerical results for symmetric travelling-wave solutions of the linearised curvature system (53)–(55), with the asymptotic analysis of Appendix A for $\varepsilon \ll 1$. (a) The maximum thickness perturbation $Y(1/2)$ against ε. (b) The scaled wave speed K against ε. (c) and (d) The thickness perturbation for $\varepsilon = 0.03$ and $\varepsilon = 0.2$ respectively. In all cases, the numerical results are shown with solid lines, leading-order asymptotic results with dot-dashed lines and the first order corrections with dashed lines.

Figure 6: The branches of periodic travelling-wave solutions to (50) and (51) with period 1. The lines show mixed-mode solutions for $\delta = 0.1$ (dashed), $\delta = 1/(4\pi)$ (dot-dashed) and $\delta = 0.07$ (dotted). Also shown are the corresponding symmetric-mode branches (continuous lines) with spatial periods $\frac{1}{2}$ and $\frac{1}{4}$, which each collapse to a single curve for all δ. The various symbols indicate points where the antisymmetric amplitude $\hat{\eta}$ tends to zero, when either η tends to zero too (circles), the branch merges with the period-$\frac{1}{2}$ symmetric branch (triangles), or the branch merges with the period-$\frac{1}{4}$ symmetric branch (squares). The small crosses indicate the locations of the solutions shown below in figure 7.

Figure 7: The deformed wall positions for four mixed-mode travelling wave solutions of (50) and (51). (a) $\delta = 0.1$, $\tilde{\eta}(0) = 0.1$, $\tilde{c} = 11.7$, (b) $\delta = 0.1$, $\tilde{\eta}(0) = 0.1$, $\tilde{c} = 13.6$, (c) $\delta = 0.07$, $\tilde{\eta}(0) = 0.2$, $\tilde{c} = 7.85$, and (d) $\delta = 0.07$, $\tilde{\eta}(0) = 0.2$, $\tilde{c} = 13.4$. These parameter choices are indicated by the small crosses in figure 6 above.

Figure 8: (a) The velocity c of the nonlinear system symmetric mode travelling waves as a function of the maximum or minimum displacements, $\eta(0)$ and $\eta(1/2)$ respectively, for varying values of δ. (b) A selection of thickness profiles for travelling solutions of the nonlinear system with $\varepsilon = 0.35$. In both cases the thin solid line is $\delta = 0.1$, the dashed line is $\delta = 0.2$ and the dot-dashed line is $\delta = 0.3$. The dotted line is the linearised curvature system velocity.

Figure 9: The evolution in time of a travelling wave from figure 2 over one time period T. Only the top interface of the channel is illustrated, with the bottom being a reflection in $\eta = 0$. The nondimensional time period is $T = 1/c = 0.08$ and the thin solid line is $t = T/4$, the dashed line is $t = T/2$, the dot-dashed line is $t = 3T/4$ and the thick solid line is $t = T$)

Figure 10: Propagation of waves with initial profiles given by (34) and (35) with $\varepsilon_s = 0.7$ and $\delta = 0.1$. In all cases the dashed line is the fully linearised profile, the dot-dashed line is the leading order curvature profile and the solid line is the full curvature profile. (a) $t = T/4$, (b) $t = T/2$, (c) $t = 3T/4$ and (d) $t = T$.

Figure 11: The axial velocity profiles associated with the wall profiles in figure 10 with $\varepsilon_s = 0.7$ and $\delta = 0.1$. In all cases the dashed line is the fully linearised profile, the dot-dashed line is the leading order curvature profile and the solid line is the full curvature profile. (a) $t = T/4$, (b) $t = T/2$, (c) $t = 3T/4$ and (d) $t = T$.

Figure 12: (a) The wall profiles as η approaches 0 for the symmetric mode. (b) The corresponding axial velocity profile. In both cases $\varepsilon_s = 0.8$, $\delta = 0.1$ and $t = 0.0241$

Figure 13: Propagation of waves with initial profiles given by (39) and (40) with $\varepsilon_a = 0.8$ and $\delta = 0.1$. In all cases the dashed line is the fully linearised profile, the dot-dashed line is the leading order curvature profile and the solid line is the full curvature profile. (a) $t = T/4$, (b) $t = T/2$, (c) $t = 3T/4$ and (d) $t = T$.

Figure 14: (a) The wall profiles as η approaches 0 for the antisymmetric mode. (b) The corresponding axial velocity profile. In both cases $\varepsilon_a = 1.25$, $\delta = 0.1$ and $t = 0.0241$

Figure 15: The deviation from the undisturbed values of the thickness with $\varepsilon_s = 0.45$ and $\delta = 1$ given by the solid line, and the centreline with $\varepsilon_a = 0.45$ and $\delta = 0.1$ given by the dashed line.

Figure 16: Propagation of waves with initial profiles given by (34), (35), (39) and (40) with $\varepsilon_a = \varepsilon_s = 0.1$ and $\delta = 0.1$. In both cases the leading order curvature profile is given by the dot-dashed line and the full curvature profile is given by the solid line. (a) $t = T/4$, (b) $t = T/2$, (c) $t = 3T/4$ and (d) $t = T$.